https://doi.org/10.5194/egusphere-2026-6669
Preprint. Discussion started: 16 November 2026
© Author(s) 2026. CC BY 4.0 License.

Evaluation of direct assimilation of brightness temperature to update Arctic sea-ice model fields

Marina Durán Moro[1], Thomas Lavergne[1], Laurent Bertino[2], Cyril Palerme[1], Yue Ying[2], Jiping Xie[2], and Atle Macdonald Sørensen[1]

[1]Norwegian Meteorological Institute, Oslo, Norway
[2]Nansen Environmental and Remote Sensing Center, 5007 Bergen, Norway

Correspondence: Marina Durán Moro (marinadm@met.no)

Abstract. Traditionally, sea-ice concentration (SIC) derived from satellite brightness temperature (Tb) observations is assimilated in operational ocean prediction systems. However, SIC is a bounded variable, which violates the Gaussian assumptions commonly used in data assimilation. Moreover, different algorithms for retrieval of sea-ice variables often introduce inconsistencies, particularly in the marginal ice zone (MIZ). Also, the valuable sea-ice age information inherent in Tb measurements is lost in the SIC product. In this study, we investigate the direct assimilation of Level-1 Tb observations from the Advanced Microwave Scanning Radiometer (AMSR2) satellite mission into an Arctic coupled ocean-sea-ice numerical model during a winter season. Since Tb is not a model variable, a radiative transfer model (RTM) is implemented, incorporating four parameterizations for the effective emissivity over sea-ice areas. These include a fixed parameterization with constant values across the region, an Atlas-based climatology parameterization, a new method based on a Distance Along the Line (DAL) computation, and a machine learning approach. We evaluate each parameterization by comparing the RTM-simulated Tbs to the AMSR2 Tbs. The DAL-based parametrization yields the best results, with mean absolute differences less than 4 K. Then, the assimilation is performed through a series of standalone analyses using the Ensemble Kalman Filter to update the sea-ice forecast fields by running five different experiments, one assimilating a high-resolution SIC product (SIRANO), and the others assimilating AMSR2 Tbs using the four different RTM parameterizations. When the resulting analyses are compared to SIRANO SIC, the DAL experiment shows the lowest differences. This is corroborated by the comparison to another SIC product (Bremen ARTIST Sea Ice). In the MIZ, the Tb-assimilation experiments demonstrate a 2–9% reduction in the mean absolute difference compared to the AMSR2 SIC observations (SIRANO and Bremen) relative to the SIC-assimilation experiment. These findings are encouraging and highlight the potential of assimilating Level-1 Tb observations to improve sea-ice analyses and forecasts.

1 Introduction

The Arctic region has experienced a significant increase in human activities over recent decades, including ship transport, tourism, oil and gas exploration, and search and rescue operations (Stocker et al., 2020; Gunnarsson, 2021; Müller et al., 2023). The ongoing decline in sea ice has increased Arctic accessibility, driving demand for accurate and reliable forecasts. In

https://doi.org/10.5194/egusphere-2026-6669
Preprint. Discussion started: 16 November 2026
© Author(s) 2026. CC BY 4.0 License.

addition to improving forecast accuracy, the timely delivery of forecasts is critical for supporting these activities. Consequently, enhancing and streamlining the production chain for Arctic sea-ice forecasts is essential.

Operational forecasting systems currently assimilate sea-ice concentration (SIC) derived from passive microwave (PMW) satellite data (Bertino et al., 2025). PMW data, a key source for SIC retrieval, measures microwave radiation emitted by Earth's surface and atmosphere at multiple frequencies and polarizations. Several SIC algorithms (Ivanova et al., 2015; Kern et al., 2019) can be applied to retrieve SIC from PMW data, using distinct Tb signatures over sea-ice and open-water areas and exploiting different combinations of frequencies and polarizations. PMW remote sensing offers consistent measurements in both day and night conditions, as well as during clear skies and cloud cover.

Among the more recent PMW missions is the Advanced Microwave Scanning Radiometer-2 (AMSR2), launched in 2012 aboard the Global Change Observation Mission - Water (GCOM-W1) satellite. Operational SIC maps derived from AMSR2 brightness temperature (Tb) data are provided by organizations such as the Ocean and Sea Ice Satellite Application Facility (OSI SAF, https://osi-saf.eumetsat.int/products/sea-ice-products) and the University of Bremen (Bremen ASI, https://seaice.uni-bremen.de/sea-ice-concentration/). The SIRANO (Sea Ice Retrievals and data Assimilation in NOrway) project recently introduced a resolution-enhancing technique to improve SIC mapping (Rusin et al., 2024).

However, SIC assimilation faces significant limitations. SIC retrievals are typically conducted by centers separate from the data assimilation (DA) and forecasting centers, creating delays and bottlenecks in the value chain. Moreover, the resulting SIC Level-3 or -4 products are averages of two to four satellite passes per day, lacking the temporal resolution of individual observations in the analyses (Durán Moro et al., 2024). Additionally, SIC is a bounded variable (0–100%), violating the Gaussian error distribution assumptions in most assimilation algorithms. In contrast, Tbs and their uncertainties exhibit a closer adherence to Gaussian distributions, avoiding information loss due to SIC capping. Importantly, raw Tb data retain ice-type information (e.g., first-year ice (FYI) versus multi-year ice (MYI)) which is lost in SIC products. To overcome these limitations, this study explores the direct assimilation of satellite Tb data.

The retrieval of SIC from Tb measurements relies on radiative transfer models (RTMs), which simulate Tb based on SIC and atmospheric fields. One widely used forward model is RTTOV (Radiative Transfer for TOVS), designed to calculate top-of-atmosphere radiances and Tbs for passive satellite instruments. RTTOV requires vertical profiles of atmospheric fields to account for the atmospheric contribution to the observed Tb. While the surface emissivity parametrization and maps embedded in RTTOV are widely used, they lack the temporal and spatial resolution needed to capture the dynamic nature of Arctic sea ice, particularly year-to-year variations. Several studies have investigated sea-ice emissivity parameterizations that distinguish between MYI and FYI ice (Mathew et al., 2009; Scarlat et al., 2017, 2020; Yan et al., 2026), as well as the use of neural networks to produce daily emissivity climatology maps (Kilic et al., 2025). However, these advanced techniques are not straightforward to implement in a DA context because they either require several auxiliary datasets that are not available from the ocean/sea-ice state, or were not tuned on the specific ocean/sea-ice forecast system we target.

Direct assimilation of Tb has shown promises in overcoming the limitations of SIC-based methods. For example, Scott et al. (2012) investigated the assimilation of AMSR-E Tb into a variational system over a FYI-dominated region near Canada. They employed a simplified RTM with two emissivity parameterizations: one using fixed FYI values (Eppler et al., 1992), and another

https://doi.org/10.5194/egusphere-2026-6669
Preprint. Discussion started: 16 November 2026
© Author(s) 2026. CC BY 4.0 License.

using sea-ice thickness (SIT) as a parameter. The latter approach yielded improved analyses compared to SIC assimilation. Simply choosing a fixed emissivity for FYI/MYI is not sufficient as demonstrated in Geer (2024), where the emissivity needs to vary substantially with the surface state. Geer (2024) developed a hybrid method combining machine learning and DA techniques. Their data-driven emissivity model, which incorporated atmospheric and sea-ice variables, successfully simulated Tbs via an RTM and optimized Tb fits to AMSR2 observations. The method of Geer (2024) was closely embedded in the ECMWF Integrated Forecast System (IFS), and thus difficult to extract for our target sea-ice forecast system. The original Geer (2024) results also exhibited a significant bias in MYI regions, which supported our independent investigations.

An Arctic coupled ocean and sea ice forecast system has been implemented by the Nansen Environmental and Remote Sensing Center (Sakov et al., 2012; Xie et al., 2017). The latest version of this system (TOPAZ5, Othmani et al. 2026) uses the HYbrid Coordinate Ocean Model (HYCOM, Bleck 2002), version 2.2.98, coupled with version 5.1 of the Los Alamos sea ice model (CICE, Hunke et al. 2015), with an horizontal resolution of ∼6 km. Since 2022, using a 100-member ensemble assimilation scheme, the Norwegian Meteorological Institute has operationally implemented it to provide 10-days forecasts for the Arctic ocean and sea ice under the Copernicus framework (Bertino et al., 2021; Ali et al., 2025; Othmani et al., 2026). A DA system combines the background (coming from the model forecast) with observations to provide an optimal estimate (the analysis) of the model states. In this study, we employ the Ensemble Kalman Filter (EnKF, Evensen 1994, 2003), in particular the Deterministic EnKF variant (DEnKF, Sakov and Oke 2008), to perform the DA analysis and update TOPAZ5 sea-ice forecasts. The DEnKF is widely applied in previous studies for coupled ice-ocean models (e.g., Cheng et al. 2023), it is also implemented in the operational TOPAZ system to provide daily forecasts in CMEMS (Sakov et al., 2012).

This study aims to improve Arctic sea-ice forecasts by directly assimilating AMSR2 Tbs using a simplified RTM (based on the Wentz and Meissner (2000)) as forward model. Originally, the Wentz and Meissner (2000) RTM covers Tb simulations over the open ocean surface and accounts for the radiative contribution of the atmosphere above. It was modified in the context of the EUMETSAT Ocean and Sea Ice Satellite Application Facility (OSI SAF) to also simulate sea ice (and mixed ocean/sea-ice) surfaces using a constant emissivity (Tonboe et al., 2016). In this study, we implement and evaluate four different sea-ice emissivity parameterizations: (i) FIXED: constant emissivity values from the Tonboe et al. (2016) RTM; (ii) ATLAS: monthly emissivity data from the RTTOV climatology database; (iii) DAL: emissivities derived via Distance Along the Line (DAL) from AMSR2 Tbs (Lavergne et al., 2019); (iv) ML: emissivities predicted by a machine learning algorithm. The study period spans six months, primarily covering the winter season. We use the SIRANO SIC as the baseline (i.e., "ground truth"). The RTM is first tested with each emissivity parameterizations against AMSR2 Tb data before performing assimilation experiments. Offline assimilation experiments are conducted using the EnKF-C software (Sakov, 2014) to update TOPAZ5 10-days forecast fields.

The article is structured into five sections. Section 2 introduces the RTM utilized in this study. Section 3 describes the datasets required for the RTM, the DA system, and the validation of results. Section 4 discusses the various sea-ice emissivity parameterizations tested and employed in the RTM. Section 5 presents and analyzes the results of the sea-ice emissivity parameterizations and their impact on the RTM Tb simulations. Subsequently, Sect. 6 describes the assimilation experiments and presents the results from the standalone DA analyses, comparing the outcomes of directly assimilating AMSR2 Tbs (using different emissivity

https://doi.org/10.5194/egusphere-2026-6669
Preprint. Discussion started: 16 November 2026
© Author(s) 2026. CC BY 4.0 License.

models) versus assimilating the SIRANO SIC retrieval product. Finally, Sect. 7 provides a comprehensive discussion and the conclusions of the study.

2 The forward model

The Tb measured by the satellite at an an incidence angle θ and at frequency f can be expressed as:

$$\mathrm{Tb}(\theta, f) = \mathrm{Tb_U}(\theta, f) + \tau(\theta, f)(\mathrm{Tb_s}(\theta, f) + \mathrm{Tb_\Omega}(\theta, f)) \quad (1)$$

with $\mathrm{Tb_U}$ the upwelling atmospheric emission, τ the total transmittance from the surface to the top of the atmosphere, $\mathrm{Tb_s}$ the radiation emitted by the surface, and $\mathrm{Tb_\Omega}$ the downwelling radiation scattered upward by the surface, as indicated in the schema in Fig. 1. In this study, we focus on the 19 GHz and 37 GHz frequencies at H/V-polarizations due to their relevance in

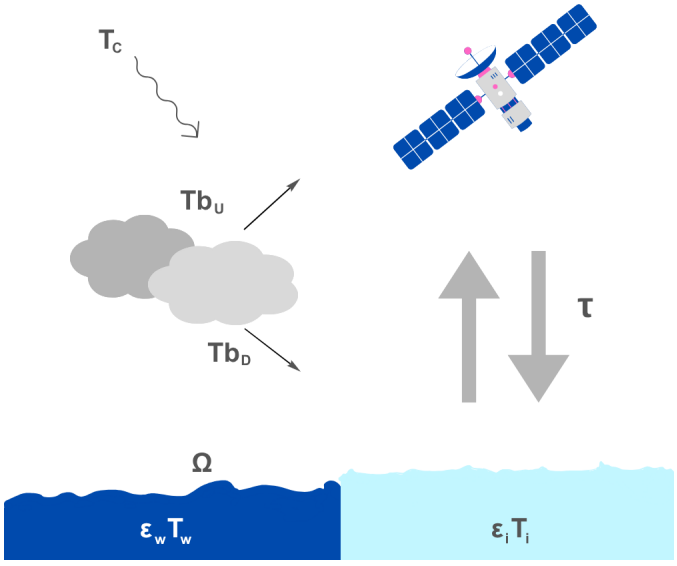


Figure 1. Schema of the physical components included in the retrieved radiative transfer model: cosmic microwave radiation ($\mathrm{T_c}$); upwelling brightness temperature ($\mathrm{Tb_U}$); effective downwelling brightness temperature ($\mathrm{Tb_D}$); atmosphere transmittance (τ); surface scattering (ω); sea-water emissivity (ϵ_w); surface water temperature ($\mathrm{T_w}$); sea-ice emissivity (ϵ_i); surface ice temperature ($\mathrm{T_i}$).

SIC algorithms (Lavergne et al., 2019; Rusin et al., 2024) and their lower sensitivity to atmospheric interactions compared to the higher frequency 89 GHz. The 89 GHz channel, with its shorter wavelength, is more susceptible to atmospheric absorption and scattering by water vapor, cloud droplets, and precipitation, which reduces its ability to penetrate the atmosphere and detect surface emissions. In contrast, the longer wavelengths of the 19 GHz and 37 GHz channels experience less atmospheric interference, making them more effective for observing surface conditions under moderate atmospheric disturbances.

https://doi.org/10.5194/egusphere-2026-6669
Preprint. Discussion started: 16 November 2026
© Author(s) 2026. CC BY 4.0 License.

The RTM (Wentz and Meissner, 2000) used in this study includes the posterior modifications on the atmospheric contribution (Meissner and Wentz, 2002, 2004, 2006, 2012). The top of atmosphere T_b is computed as:

$$\mathrm{Tb}(\theta,f) = \mathrm{Tb_U}(\theta,f) + \tau(\theta,f)(1-\mathrm{SIC})\epsilon_\mathrm{w}(\theta,f)\mathrm{T_s} + \tau(\theta,f)\mathrm{SIC}\epsilon_\mathrm{i,eff}(f)\mathrm{T_i}(f) + \tau(\theta,f)\mathrm{Tb}_{\Omega,\mathrm{w}}(\theta,f) + \tau(\theta,f)\mathrm{Tb}_{\Omega,\mathrm{i}}(\theta,f) \quad (2)$$

with ϵ_w the sea water emissivity, $\epsilon_\mathrm{i,eff}$ the sea-ice effective emissivity, $\mathrm{T_s}$ the skin temperature, $\mathrm{T_i}$ the ice temperature, and $\mathrm{Tb}_{\Omega,\mathrm{w}}(\theta,f)$ and $\mathrm{Tb}_{\Omega,\mathrm{i}}(\theta,f)$ the sea water and ice reflected downwelling contributions, respectively. These two terms include $\mathrm{Tb_D}$ among others (see details in Wentz and Meissner (2000)).

In the RTM implemented for this study, T_i is approximated as T_s in the surface contribution, simplifying the model by using the skin temperature (T_s) to represent sea ice emission. However, this is an approximation, as in reality, the radiation emitted by sea ice originates from within its structure, including the sea ice and snow layers. This emission is influenced by several factors, such as microwave frequency, sea ice type, snow depth, and snow grain size. Consequently, the use of T_s implies that $\epsilon_\mathrm{i,eff}$ represents an effective emissivity for the combined sea ice and snow cover, rather than the true physical emissivity. While the true emissivity cannot exceed unity, it is occasionally the case for the effective emissivity.

Sea-water emissivities (ϵ_w) are calculated in the RTM using the Fresnel equations, which depend on the dielectric properties of sea water. Additional corrections are applied to account for surface roughness caused by wind and the increased emissivity resulting from foam at higher wind speeds (Wentz and Meissner, 2000). In order to compute the terms ϵ_w, τ, $\mathrm{Tb_U}$, and $\mathrm{Tb_D}$ in Eq. 2, atmospheric data are needed. These are presented in Sect. 3.

For effective sea-ice emissivities ($\epsilon_\mathrm{i,eff}$), we explore various parameterizations to implement in the RTM, which are detailed in Sect. 4. Following Prigent et al. (1997), the effective emissivities can be calculated from observed Tbs and atmospheric fields by applying the following equation:

$$\epsilon_\mathrm{eff}(\theta,f) = (\mathrm{Tb}(\theta,f) - \mathrm{Tb_U}(\theta,f) - \tau(\theta,f)\mathrm{Tb_D}(\theta,f))/(\tau(\theta,f)(\mathrm{T_s} - \mathrm{Tb_D}(\theta,f))) \quad (3)$$

3 Data

This section outlines the data utilized for forward model evaluation and standalone analysis, during the period from November 2023 to April 2024.

3.1 Forward model input data

The forward model simulates Tb for the selected channel and incidence angle. The selected frequencies for this study are 19 and 37 GHz at each H/V-polarization. To perform the RTM Tb simulation, a series of atmospheric fields are required: (i) columnar water vapor (mm); (ii) columnar cloud liquid water (mm); (iii) wind speed over water (m/s); (iv) surface temperature (K) at 2 meters. These atmospheric fields are provided by ECMWF Reanalysis v5 (ERA5) produced by the Copernicus Climate Change Service (C3S) at ECMWF (Hersbach et al., 2023). The inclination angle is required in the RTM which is provided by AMSR2 data (∼55 degrees). Another input parameter is the SIC, which corresponds to AMSR2 SIC (see Subsect.3.3) during forward

https://doi.org/10.5194/egusphere-2026-6669
Preprint. Discussion started: 16 November 2026
© Author(s) 2026. CC BY 4.0 License.

model validation and to TOPAZ5 SIC (see Subsect.3.2) in the standalone analysis. Before being used in the forward model, the atmospheric and AMSR2 fields are projected onto the TOPAZ5 numerical grid.

3.2 Background ensemble data

In the EnKF approach, an ensemble of model forecasts is used as background information, with sample statistics providing a flow-dependent estimate of model state uncertainties. In this study, the 10-day forecast data from TOPAZ5, provided by CMEMS ($https://data.marine.copernicus.eu/product/ARCTIC_ANALYSISFORECAST_PHY_002_001$), is used to construct the background ensemble for each standalone analysis. The ensemble consists of 10 members, specifically taken from the forecast on the 10th day. The background ensemble includes SIC and SIT model variables. When assimilating AMSR2 Tb, the RTM-simulated Tbs are also included in the background ensemble.

3.3 Observations used for assimilation

PMW satellite AMSR2 SIC and Tb data are assimilated to update the background model ensemble in different assimilation experiments. Figure 2 illustrates the surface Tbs observed by AMSR2 on 15 January 2024. With respect to AMSR2 SIC, the SIRANO SIC product (Rusin et al., 2024) is selected (see example in Fig. A1a). This product employs a resolution-enhancement technique that generates SIC maps with higher spatial resolution compared to those produced by the standard OSI SAF algorithm.

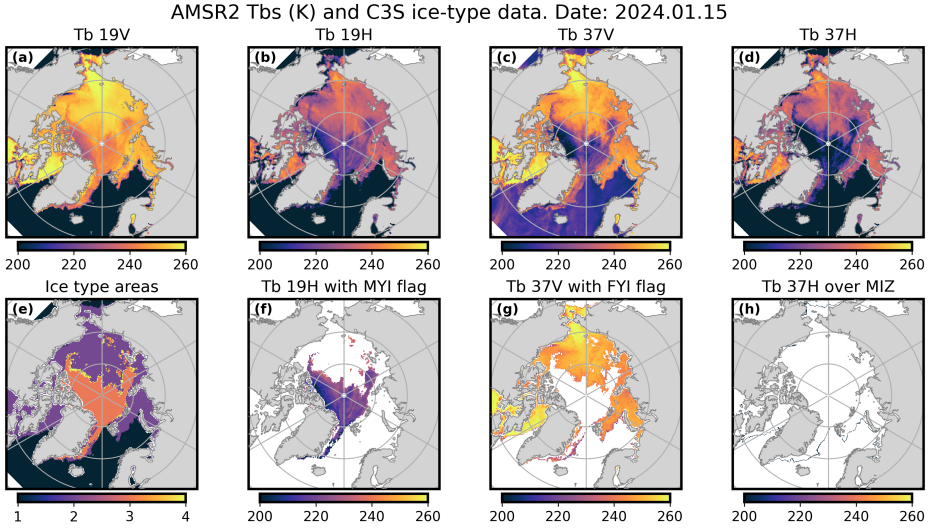


Figure 2. AMSR2 brightness temperature (Tb) maps from the 19V, 19H, 37V, and 37H channels (a-d). Daily gridded Level-4 ICDR product derived from AMSR2 data (e). Application of ICDR multi-year ice (MYI) (f) and first-year ice (FYI) (g) flags to the AMSR2 SIC fields for the 19H and 37V channels, along with marginal ice zone (MIZ) areas (h) identified on the 37H Tb map. All maps correspond to 15 January 2024.

https://doi.org/10.5194/egusphere-2026-6669
Preprint. Discussion started: 16 November 2026
© Author(s) 2026. CC BY 4.0 License.

3.4 Observations used for validation

Bremen ASI (ARTIST Sea Ice) SIC product (see example in Fig. A1b) based on AMSR-E and AMSR2 Tb data is used as a validation dataset to evaluate the assimilation results. It relies on the 89 GHz frequency channels from both AMSR-E and AMSR2 sensors. This product uses the ASI algorithm (Spreen et al., 2008). More details on the processing of the raw Tb data can be found in the University of Bremen ASI User Guide (Melsheimer, 2024).

3.5 C3S ice-type data

To assess the differences in results across various sea-ice types, we access the daily gridded L4 Sea Ice Type Interim Climate Data Record (ICDR) from the Copernicus Climate Change Service (C3S) (Aaboe et al., 2026). This dataset is derived from SSMIS data and starts in January 2020. The processing chain involves the following steps: (i) correction of atmospheric noise using a RTM; (ii) dynamic tuning of algorithms with daily updated training data; (iii) sea-ice classification based on a Bayesian approach; (iv) post-processing analysis; (v) computation of per-pixel uncertainties and status flags.

Northern Hemisphere sea ice type classification is restricted to the winter months (October to April) due to classification challenges during ice surface melting. During the summer period (May 1 to September 30), all ice is classified as ambiguous.

As an example, we show in Fig.2e the daily gridded ICDR on 15 January 2024. The following maps in this figure show the application of ICDR MYI and FYI flags on the corresponding AMSR2 Tb fields, and the last map presents the area corresponding to the marginal ice zone (MIZ) in Tb 37H field. We define in this study the MIZ as the area with SIC between 15% and 30% in the SIRANO SIC field on the specific date.

4 Effective emissivity parameterization over sea-ice areas

This study examines four different effective emissivity parameterizations for sea-ice covered areas, which are introduced and evaluated in this section. These parameterizations are implemented and tested within the RTM framework. We begin with a brief overview of the FIXED and ATLAS parameterizations, followed by a more detailed discussion of the implementation of DAL and ML effective emissivity parameterizations in subsequent subsections.

4.1 FIXED and ATLAS parameterizations

The FIXED effective emissivity parameterization assigns a constant emissivity value to sea-ice-covered areas for each channel: 0.95 (19V), 0.90 (19H), 0.93 (37V), and 0.88 (37H). This parameterization lacks both spatial and temporal variability, applying uniform values across the domain.

The ATLAS effective emissivities are derived from the monthly climatology supplied by TELSEM2 (Tool to Estimate Land Surface Emissivity from Microwave to Submillimetre Waves; Aires et al. 2011; Wang et al. 2017). TELSEM2 delivers a monthly dataset of effective emissivities spanning the 5–700 GHz frequency range, based on satellite-derived emissivities from multiple instruments. For this study, the emissivity climatology values were extracted onto the TOPAZ5 grid for each

https://doi.org/10.5194/egusphere-2026-6669
Preprint. Discussion started: 16 November 2026
© Author(s) 2026. CC BY 4.0 License.

month at 19 and 37 V/H-polarisation frequencies (see Fig.A2). The ATLAS parameterization assigns values greater than 0 up to 1 for sea-ice-covered areas and a value of zero for open-water areas. A significant limitation of the ATLAS parameterization is its insufficient data coverage near ice edges during the winter period. As a result, the ATLAS emissivity is often set to zero in ice-covered regions near the ice edge, which is a major drawback of this approach. Additionally, the TELSEM2 effective emissivities used in this application are clipped at 1, limiting their dynamic range over sea ice. This is notable because, unlike true physical emissivities, effective emissivities can exceed 1. Furthermore, TELSEM2 effective emissivities were originally derived using ERA-Interim skin temperatures, while this study applies them with ERA5 skin temperatures, which introduces a potential mismatch and is not optimal.

4.2 DAL-based parameterization

Effective emissivities are computed in a 2D plane as a function of a quantity called Distance Along the Line (DAL), first introduced by Lavergne et al. (2019), and the surface temperature from ERA5. DAL is calculated from satellite Tbs from three channels (19V, 37V, and 37H). In this three-dimensional Tb space, the Tb data for consolidated ice primarily cluster along a line referred to as the consolidated ice line, defined by the corresponding unit vector. Typically, the MYI signature appears at lower Tb values (left of the ice line), while FYI and young sea ice cluster at higher Tb values (right of the ice line) (Comiso, 2012).

The unit vector is determined using principal component analysis and represents the direction of maximum variance within the closed-ice Tb samples. DAL is then computed as the projection of the Tb vector onto the unit vector, such that DAL corresponds to the quantity given by their dot product. Since the unit vector points from MYI to FYI in the Tb space, older ice has lower DAL values than younger ice.

The coefficients of the 2D plane are updated daily using the following steps:

1. Daily dynamical samples for SIC computations are collected. From these samples, AMSR2 Tb and ERA5 data for closed-ice conditions (SIC=100%) are retrieved for use in subsequent computations.

2. Computation of effective emissivities for the dynamical samples using Eq. 3. This calculation uses AMSR2 Tb, ERA5 fields (columnar water vapor, columnar cloud liquid water, and surface temperature at 2 meters), and the AMSR2 inclination angle.

3. Calculation of DAL from AMSR2 Tb data from the dynamical samples.

4. Determine 2D plane coefficients relating effective emissivities to DAL and surface temperature. A 2D plane, $z = ax_1 + bx_2 + c$, is fitted using surface temperature (x_1) and computed DAL (x_2) from the dynamical samples, where z represents the effective emissivity, and a, b, and c are the derived coefficients.

We assume this 2D plane relationship applies across the entire sea-ice area. First, DAL is calculated on the TOPAZ5 grid using AMSR2 Tbs. Then, daily coefficients are used to derive the 2D effective emissivity field from DAL and surface temperature across the numerical domain.

https://doi.org/10.5194/egusphere-2026-6669
Preprint. Discussion started: 16 November 2026
© Author(s) 2026. CC BY 4.0 License.

4.3 ML-based parameterization

A data-driven model is developed for predicting the surface emissivities over sea ice at 19 and 37 GHz at each H/V-polarization from TOPAZ5 data. The model is trained using retrievals from AMSR2 data representing the surface emissivities (see Eq. 3), with the atmospheric contribution evaluated and removed during the estimation process of surface emissivities. The predictors from TOPAZ5 are the sea-ice age and thickness, the snow depth, as well as the x and y cartesian coordinates on the stereographic grid from TOPAZ5. In addition, the sine and cosine of the day of year are used to provide seasonal information to the neural network. The data-driven model consists of a multi-layer perceptron with 7 predictors, 3 hidden layers with widths of 16, 32, and 16 nodes, and 4 predicted variables. The model is trained using the period October 2021 to April 2023 and only data during the dry season (October to April) is used, and the period October 2023 to April 2024 is used for validation. The data from May to September is not used due to a significantly lower correlation between the surface emissivities and the sea ice type when melt-ponds are present. Only data where TOPAZ5 indicates a SIC higher than 99% were used in order to predict the sea ice emissivities (and not a combination of sea ice and water emissivities). The model is trained over 50 epochs with an initial learning rate of 0.005 which is then divided by 2 every 10 epochs.

Since the data-driven model is trained on TOPAZ5 data, it only covers the spatial grid points within the model's domain, excluding some coastal areas captured by observations. However, this is not a limitation for the assimilation study, as the RTM Tb simulations for all parameterizations are already constrained by the TOPAZ5 SIC field.

5 Evaluation of the forward model

This section evaluates the RTM's performance as the forward model over a six-month period (November 1, 2023, to April 30, 2024). The RTM simulations use AMSR2 data (SIC and effective incidence angle) and ERA5 atmospheric fields as inputs. Four RTM configurations (FIXED, ATLAS, DAL, and ML) are assessed, each utilizing a different sea-ice emissivity parameterization. During Tb simulations, the RTM applies the selected sea-ice emissivity parameterization for sea-ice-covered areas and calculates sea-water emissivity for open-water regions.

We begin by evaluating the performance of the four sea-ice emissivity parameterizations and their corresponding RTM-simulated Tbs for a specific date, followed by an assessment over the entire study period. The evaluation is limited to regions with SIC > 0% since the RTM uses a uniform water emissivity, yielding identical results in areas with zero SIC regardless of the sea-ice parameterization.

Since the ML sea-ice emissivities are confined to regions with sea-ice coverage represented in the training data, a mask is applied to limit the other parameterized emissivities and RTM Tbs to the same region. This ensures a fair and consistent comparison across all parameterizations.

https://doi.org/10.5194/egusphere-2026-6669
Preprint. Discussion started: 16 November 2026
© Author(s) 2026. CC BY 4.0 License.

5.1 Comparison of parameterized surface effective emissivities

In this subsection, we evaluate the surface effective emissivity produced by each parameterization. To account for fractional sea-ice coverage within each grid cell, the surface effective emissivity field is multiplied by SIC, resulting in a SIC-weighted field that represents the contribution of sea ice to the total grid-cell emissivity.

245 The surface effective emissivity fields for 15 January 2024 are shown in Fig. 3. Although these maps represent a single day, they are broadly representative of the entire study period, which predominantly spans a winter season. Table 1 summarizes mean surface effective emissivities over the six-month period for different sea-ice-covered regions, including the total area (All), as well as ice-type regions (MYI, FYI) and the MIZ, as defined in Sect. 3.3. The ice-type regions for 15 January 2024 are illustrated in Fig. 2, which, like the emissivity maps, is representative of the entire study period.

Channel	**19V**	**19H**	**37V**	**37H**	**19V**	**19H**	**37V**	**37H**	**19V**	**19H**	**37V**	**37H**	**19V**	**19H**	**37V**	**37H**
	All				**MYI**				**FYI**				**MIZ**			
FIXED	0.86	0.81	0.84	0.80	0.93	0.88	0.91	0.86	0.88	0.84	0.87	0.82	0.21	0.20	0.21	0.19
ATLAS	0.87	0.79	0.81	0.74	0.92	0.83	0.80	0.73	0.91	0.83	0.87	0.79	0.19	0.14	0.19	0.15
DAL	0.91	0.84	0.87	0.81	0.96	0.87	0.86	0.79	0.94	0.87	0.93	0.87	0.22	0.20	0.22	0.20
ML	0.91	0.84	0.86	0.81	0.96	0.88	0.86	0.80	0.94	0.88	0.91	0.86	0.22	0.21	0.22	0.20

Table 1. Mean surface effective emissivities averaged over a six-month period (1 November 2023 – 30 April 2024) for FIXED, ATLAS, DAL, and ML parameterizations and for each channel (19V, 19H, 37V, 37H). It is computed for different regions: All (total area), MYI (multi-year ice), FYI (first-year ice), and MIZ (marginal ice zone).

https://doi.org/10.5194/egusphere-2026-6669
Preprint. Discussion started: 16 November 2026
© Author(s) 2026. CC BY 4.0 License.

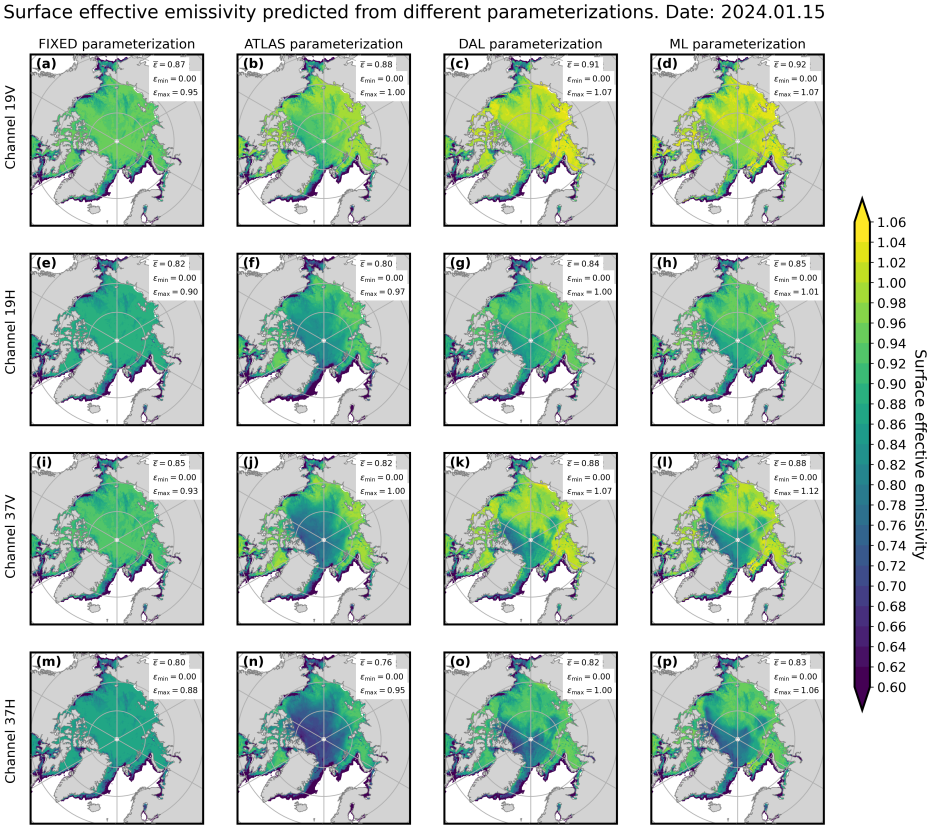


Figure 3. Maps of simulated surface effective sea-ice emissivity on 2024-01-15 for FIXED, ATLAS, DAL, and ML parameterizations (columns) across channels 19V (a–d), 19H (e–h), 37V (i–l), and 37H (m–p), with the mean, minimum, and maximum values displayed in the top-right corner of each panel.

The emissivity maps exhibit a wide range of values, spanning from very low values (<0.6) in the MIZ to values close to or exceeding 1 in FYI areas, depending on the parameterization. The lowest emissivity values (close to 0) are observed near the MIZ, where open water dominates (SIC $\sim 0\%$).

DAL and ML parameterizations clearly distinguish between MYI and FYI areas, with the 37V channels showing the sharpest contrast between these regions. These parameterizations effectively capture the emissivity differences, with lower values over MYI and higher values over FYI, where maximum emissivities exceed 1 in the V-channels for DAL and across all channels for ML. The lowest MYI emissivity values are observed in the 37H channels for both DAL and ML, as well as for ATLAS. The mean effective emissivities over the total area (see Tab. 1) reveal that DAL and ML parameterizations consistently produce higher values compared to FIXED and ATLAS. For all parameterizations, 19V channel presents highest mean emissivities, which is consistent with mean emissivity values in MYI and FYI areas, where this channel presents higher means.

The ATLAS parameterization also demonstrates some differentiation between ice types across all channels, though less distinctly compared to DAL and ML. Low emissivity values extend over a larger area in the Amerasian Basin, particularly in

https://doi.org/10.5194/egusphere-2026-6669
Preprint. Discussion started: 16 November 2026
© Author(s) 2026. CC BY 4.0 License.

the Canadian Basin, impacting both MYI and FYI areas. In certain regions near the MIZ (mainly along the Greenland and Barents Sea, and Svalbard coastal area) some ATLAS emissivity values are either low or set to zero due to its reliance on a monthly climatology, which lacks data coverage for these areas. Therefore, ATLAS mean emissivities are generally lower compared to other parameterizations, particularly for H-channels in the MIZ.

The FIXED parameterization, which assumes a constant sea-ice emissivity, generates surface effective emissivity fields primarily influenced by SIC. This is especially evident in regions with high SIC, leading to a more uniform distribution. Compared to DAL and ML, FIXED overestimates MYI mean emissivities at 37 GHz and underestimates FYI mean emissivities across all channels.

In the MIZ, FIXED produces mean emissivities similar to but slightly lower than those of DAL and ML. In this region, where low SIC increases the contribution of water emissivity, the mean emissivity values for all parameterizations are generally around 0.2, except for ATLAS, which is affected by its lack or absence of effective sea-ice emissivity values in the climatology.

5.2 Evaluation of RTM Tbs from each parameterization

Figures 4 and 5 compare RTM-simulated Tbs with AMSR2 Tbs and their differences for January 15, 2024, across parameterizations and channels. The simulated Tbs closely follow surface emissivity patterns (Fig. 3) across all parameterizations. ATLAS, DAL, and ML exhibit lower Tbs in MYI regions and higher Tbs in FYI regions, while V-channels consistently show higher Tbs than H-channels, reflecting the elevated emissivity in FYI regions.

FIXED, using a constant emissivity value, does not distinguish between ice types and produces higher Tbs in V-channels. ATLAS, however, shows unrealistically low values in the MIZ, particularly in the 37V channel, due to missing emissivity data. For all parameterizations except ATLAS, the minimum Tbs are consistent across channels: approximately 185 K for 19V, 100 K for 19H, and 134 K for 37H, with DAL showing the lowest minimum for 37V. Maximum Tbs are observed in FYI regions, generally above 240 K for all channels and parameterizations.

The differences in RTM-simulated and AMSR2 Tbs (Fig. 5) highlight parameterization performance. DAL achieves the lowest MAD values across all channels, particularly in V-channels, followed by ML. ATLAS outperforms FIXED in V-channels by capturing FYI and MYI contrasts but shows high MAD values in the MIZ due to missing emissivity data. FIXED struggles most, particularly in MYI regions, with large differences in the 37V and 37H channels.

Difference patterns reveal specific issues: FIXED overestimates Tbs in MYI and underestimates them in FYI areas, especially in V-channels. ATLAS underestimates Tbs in FYI and MIZ areas, with the largest discrepancies in H-channels. DAL shows consistently low differences, with minor overestimations near the MIZ, while ML performs well overall but slightly overestimates Tbs near the MIZ and underestimates them in scattered MYI and FYI regions.

Over six months, the difference patterns for FIXED and ATLAS remain stable, while DAL consistently shows low differences. ML exhibits dynamic patterns, with recurring overestimations in the Greenland Sea extending toward the Eurasia Basin.

Figure 6 summarizes the six-month MAD trends across regions. DAL consistently achieves the lowest MAD (< 3.50 K) for all channels, with the best performance (< 1.50 K) in the 37V channel. ML performs slightly worse (< 7 K), excelling in the

https://doi.org/10.5194/egusphere-2026-6669
Preprint. Discussion started: 16 November 2026
© Author(s) 2026. CC BY 4.0 License.

19V channel but struggling in the 37H channel. FIXED performs best in the 19H channel ($\sim 8K$) but deteriorates in the 37V channel (> 12 K) due to sharp regional contrasts. ATLAS achieves its lowest MAD in the 19V channel ($< 10K$) but exhibits significantly higher MAD (> 14 K) in the 37H channel due to widespread underestimations.

Across subregions, DAL remains the best-performing parameterization, followed by ML. In the MIZ, differences between parameterizations narrow (< 6 K), except for ATLAS, where missing climatology data leads to higher MAD values (6-15 K). In MYI areas, DAL shows higher MAD for V-channels compared to FYI areas due to localized differences in North Greenland and Canadian regions. H-channel differences are more evenly distributed across ice types. ML's highest MAD values occur in the 37 channels due to mixed errors near the North Canadian and Greenland coasts. In contrast, ATLAS exhibits consistently high MAD values (> 9 K) for both MYI and FYI areas, performing best in the 19V channel. FIXED shows particularly high MAD values (> 13 K) in MYI regions for 37 channels due to overestimations, while FYI underestimations lead to MAD values exceeding 9 K across all channels.

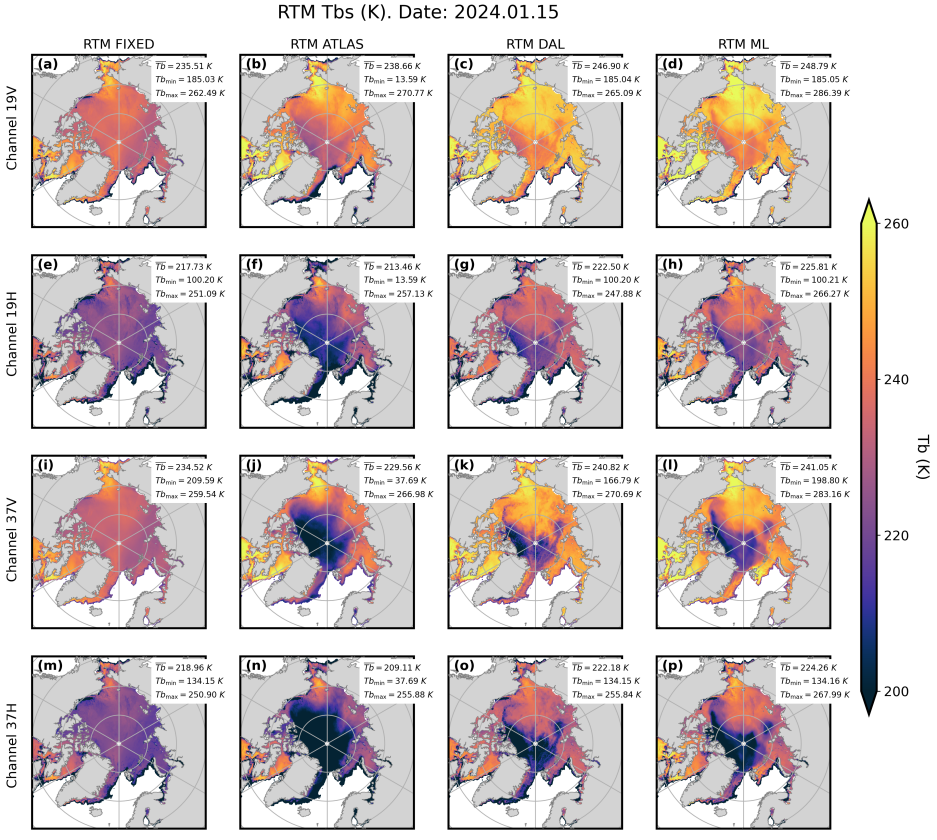


Figure 4. Maps of RTM Tbs on 2024-01-15 for FIXED, ATLAS, DAL, and ML parameterizations (columns) across channels 19V (a–d), 19H (e–h), 37V (i–l), and 37H (m–p), with the mean, minimum, and maximum Tb values displayed in the top-right corner of each panel.

https://doi.org/10.5194/egusphere-2026-6669
Preprint. Discussion started: 16 November 2026
© Author(s) 2026. CC BY 4.0 License.

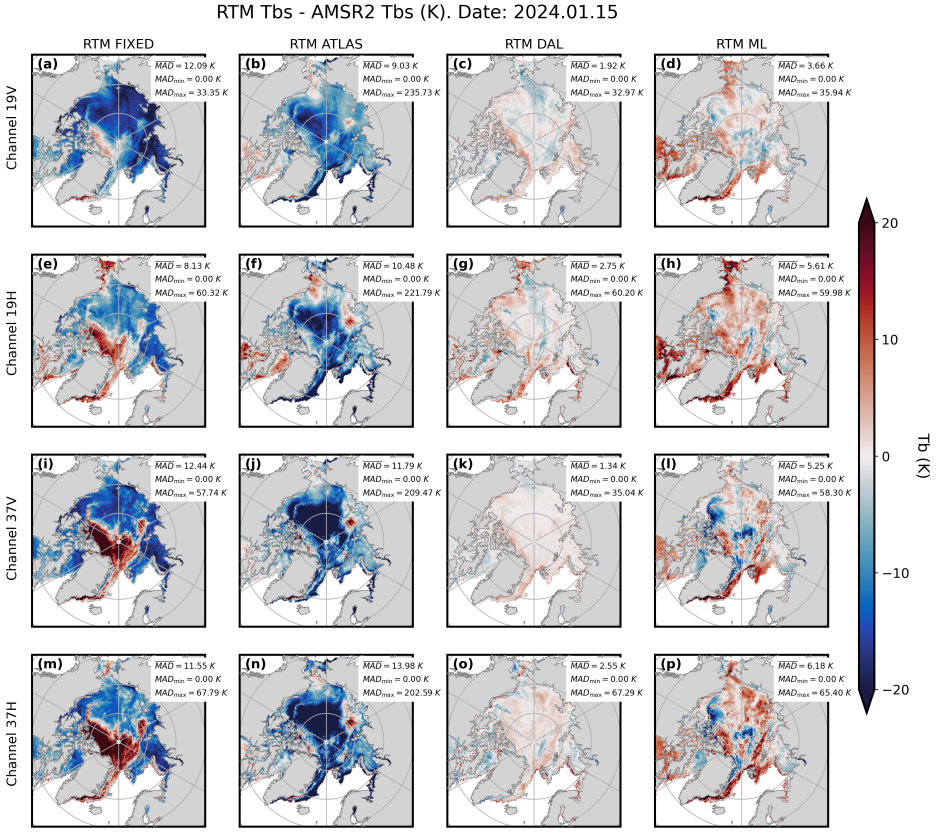


Figure 5. Maps of the difference between simulated RTM and observed AMSR2 Tbs on 2024-01-15 for FIXED, ATLAS, DAL, and ML parameterizations (columns) across channels 19V (a–d), 19H (e–h), 37V (i–l), and 37H (m–p), with the mean, minimum, and maximum values of the absolute difference displayed in the top-right corner of each panel.

https://doi.org/10.5194/egusphere-2026-6669
Preprint. Discussion started: 16 November 2026
© Author(s) 2026. CC BY 4.0 License.

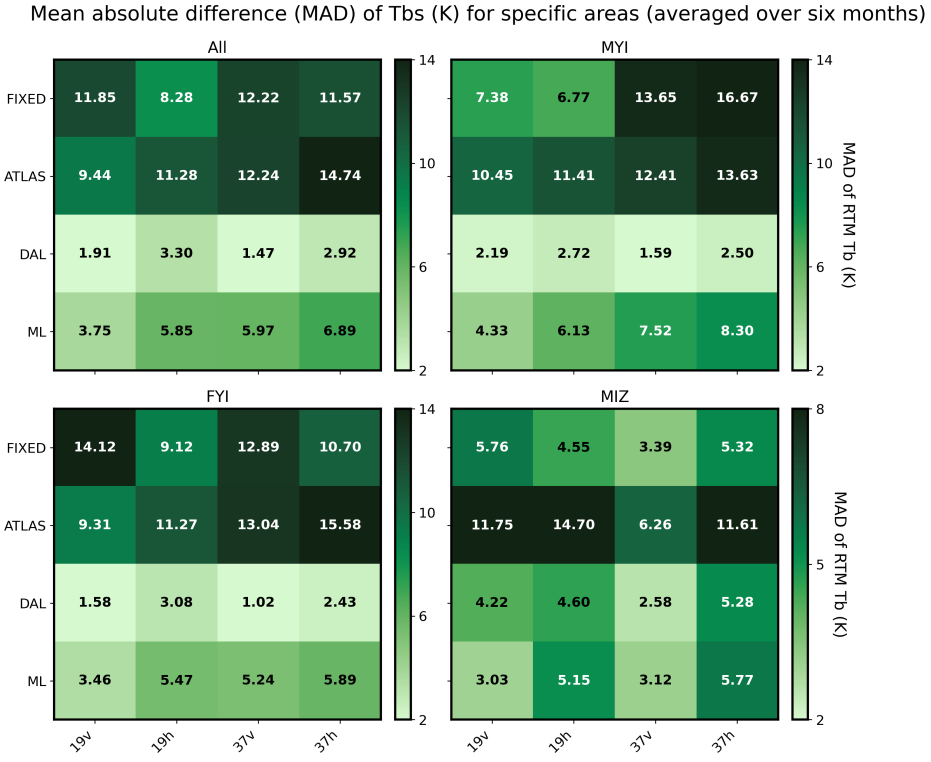


Figure 6. Heatmaps showcasing the mean absolute difference (MAD) of RTM Tbs from the FIXED, ATLAS, DAL, and ML parameterizations relative to AMSR2 Tbs over a six-month period. Each heatmap represents the MAD of Tbs across different regions: total area (All), multi-year ice (MYI), first-year ice (FYI), and marginal ice zone (MIZ), for all channels.

Figure 7 illustrates the time series of spatially averaged MAD between RTM-simulated Tbs and AMSR2 Tbs for each parameterization and channel. The results highlight the consistent daily outperformance of the DAL parameterization across all channels.

ML consistently shows higher MAD values, 2–4 K above DAL, with the smallest difference in the 19V channel where results are closest. ATLAS outperforms FIXED in the 19V channel and partially in the 37V channel, but after mid-February, FIXED surpasses ATLAS, indicating improved performance by FIXED.

Channel-specific trends reveal the smallest MAD differences in 19H, due to FIXED's relatively stronger performance, while the largest differences occur in 37V, driven by DAL's superior results.

https://doi.org/10.5194/egusphere-2026-6669
Preprint. Discussion started: 16 November 2026
© Author(s) 2026. CC BY 4.0 License.

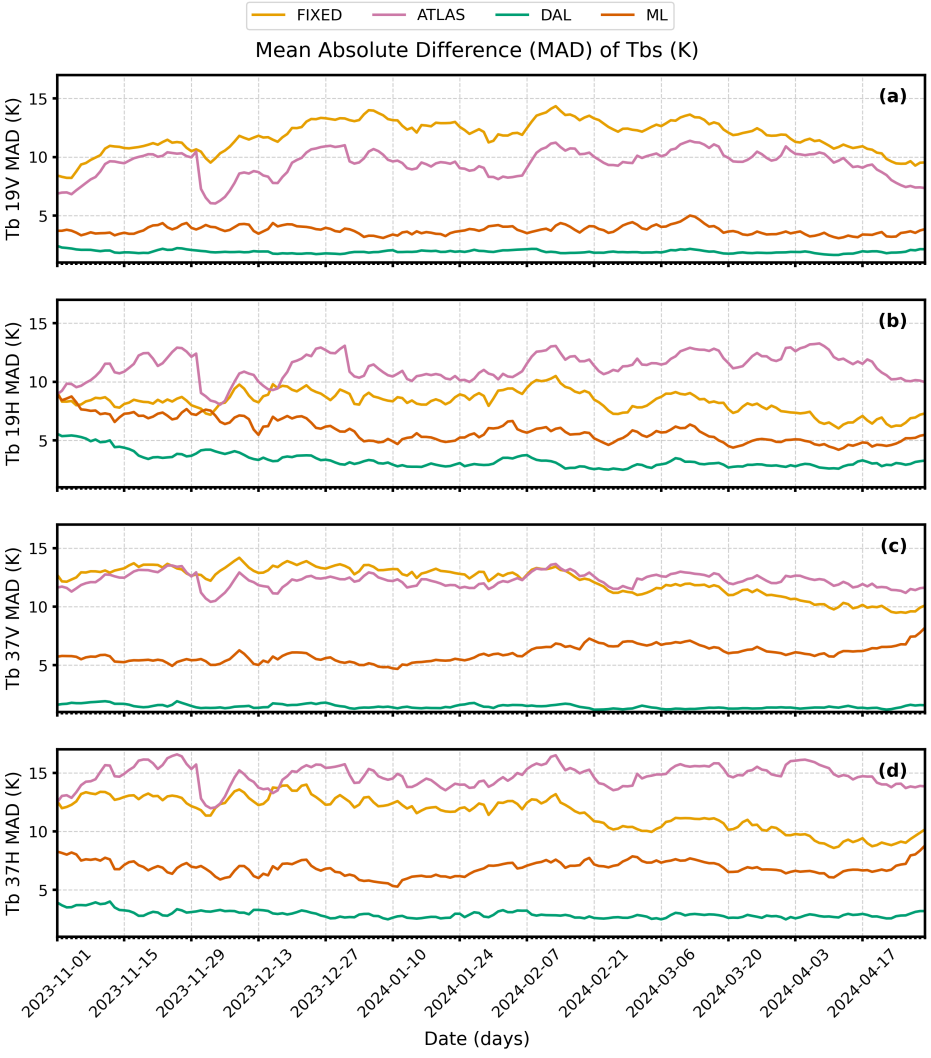


Figure 7. Time series of spatially averaged Mean Absolute Differences (MAD) between RTM-simulated Tbs and AMSR2-observed Tbs for each channel: (a) 19V, (b) 19H, (c) 37V, and (d) 37H. The MAD values are computed over the six-month period from November 2023 to April 2024.

315 Figure 8 shows 2-dimensional scatter plots comparing RTM-simulated Tbs with AMSR2 Tbs over six months in sea ice-covered areas (SIC $\geq 95\%$). The plots evaluate relationships between the 19V and 37V channels (left) and the 37H and 37V channels (right). Each subplot represents a specific parameterization, with the AMSR2 scatter cloud (gray) as a reference. MYI data appear on the left (lower Tbs) of the AMSR2 cloud, while FYI data are on the right (higher Tbs). Mean values and key statistics (e.g., MAD, RMSD, and correlation) are included in each plot.

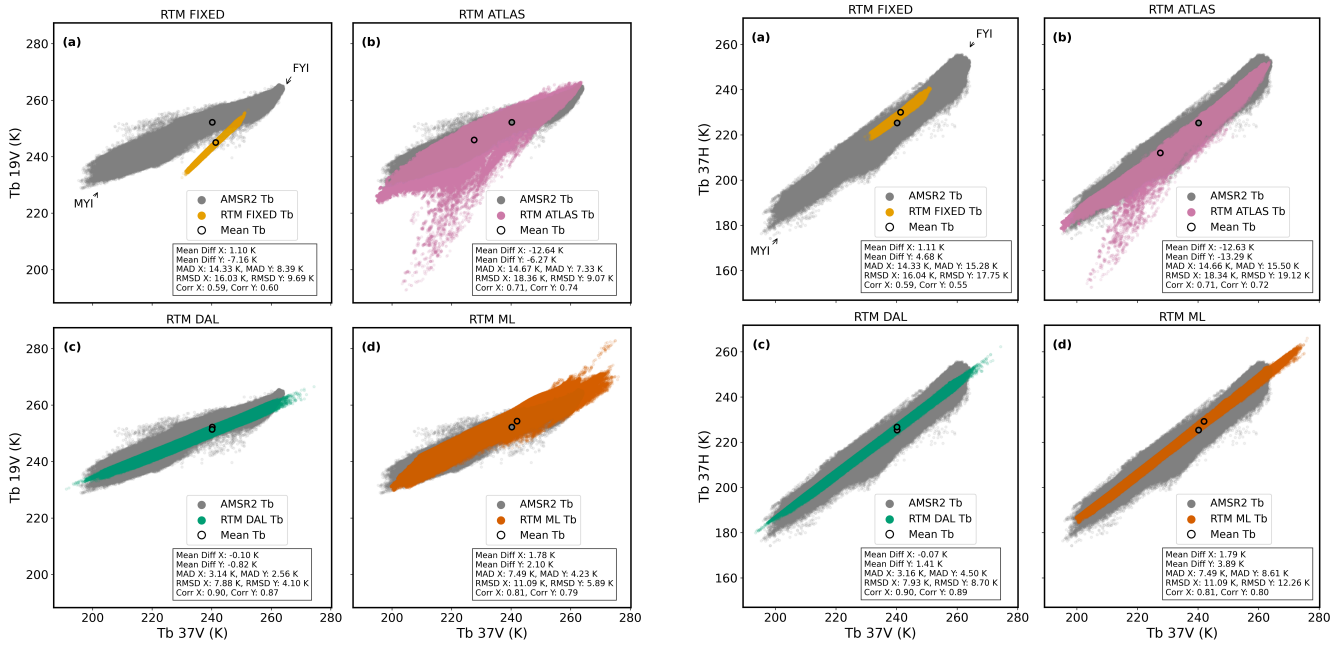
https://doi.org/10.5194/egusphere-2026-6669
Preprint. Discussion started: 16 November 2026
© Author(s) 2026. CC BY 4.0 License.

- FIXED: Displays poor alignment with AMSR2 (corr ~ 0.60). In the 19V-37V diagram, FYI Tbs are underestimated, while MYI Tbs show overestimation in the 37V channel but better agreement in 19V. For 37H-37V, MYI Tbs are strongly overestimated, while FYI Tbs are slightly underestimated. Overall, FIXED demonstrates weak performance with large discrepancies.

- ATLAS: Shows improved alignment (corr > 0.70) compared to FIXED but suffers from consistent underestimation. Misaligned points in the lower left-hand corner highlight underestimation in FYI (e.g., Amerasian Basin) and some MYI areas. Despite better alignment, significant misalignment from the AMSR2 cloud remain.

- DAL: Achieves the strongest performance (corr ~ 0.90), with low MAD (< 5 K) and RMSD (< 8 K). Most DAL Tbs fall within the AMSR2 cloud, with similar mean values, indicating good agreement. While maximum and minimum values slightly exceed the AMSR2 range, alignment remains robust.

- ML: Demonstrates high correlation (corr ~ 0.80), though slightly below DAL. ML aligns well with AMSR2 but tends to overestimate Tbs, especially in FYI areas, as reflected in the higher mean values and right-side extremes. The ML scatter cloud is more spread out than DAL in the 19V-37V diagram but remains well-aligned overall.



(a) (b)

Figure 8. Scatter diagrams of AMSR2 (gray) and RTM (colors) Tbs over areas with SIC $> 95\%$ (FIXED: orange (a), ATLAS: pink (b), DAL: green (c), ML: orange (d)). Left figure: Tbs 19V (axis y) in function of Tbs 37V (axis-x), right figure: Tbs 37H (axis y) in function of Tbs 37V (axis-x). The circle marker indicates the mean of Tbs for each dataset. Right bottom box presents statistics of Tbs comparing both datasets.

https://doi.org/10.5194/egusphere-2026-6669
Preprint. Discussion started: 16 November 2026
© Author(s) 2026. CC BY 4.0 License.

The Tb distributions over areas with SIC greater than 50% are presented in the Appendix (see Fig. A3). DAL and ML parameterizations show RTM Tb distributions that closely match the AMSR2 Tb distributions, indicating a better representation of both FYI and MYI Tb values by these parameterizations, with DAL performing particularly well.

6 Comparison of assimilation of Tbs versus SIC

6.1 Experiments design

For the assimilation of AMSR2 Tbs, results are shown using the four RTM versions, each employing a different sea-ice parameterization (see details in Tab. 2). Over the analysis period from 1 November 2023 to 30 April 2024, a total of 182 standalone experiments were conducted. In all experiments, the DEnKF parameters were configured consistently, with the observation error inflation factor (Rfactor) set to 2 and the localization radius set to 50 km. The standard error is set to 0.04 for SIC data and 10 K for Tb data (same for all channels and polarizations).

Experiment name	**CTRL**	**FIXED**	**ATLAS**	**DAL**	**ML**
Observation assimilated	SIRANO SIC	AMSR2 Tb	AMSR2 Tb	AMSR2 Tb	AMSR2 Tb
RTM version	-	RTM FIXED	RTM ATLAS	RTM DAL	RTM ML

Table 2. Summary of assimilation experiments, including the experiment names, the corresponding observations assimilated (SIRANO SIC product or AMSR2 Tb), and the Radiative Transfer Model (RTM) version applied.

6.2 General evaluation of the analysis

Figure 9 presents maps of SIC differences between the model analysis and SIRANO SIC, SIC increments (model - analysis), SIC spread, Tb 19V background spread, and background differences relative to AMSR2 Tbs for a specific date, 2024-01-15. The results on this date are representative of the entire study period, as there are no significant variations in outcomes or spatial patterns.

The first column of maps (Fig. 9a-f) illustrates the SIC differences from the SIRANO SIC for the mean background and analysis ensembles across all experiments. The background difference map highlights a general overestimation by the model along the ice edges (red areas). The analysis, with MAD < 0.025 in all experiments (except ATLAS), significantly reduces the background differences (where MAD $= 0.036$) relative to the SIRANO SIC observations. Among the experiments, CTRL and DAL yield comparable results, while ML and FIXED achieve slightly smaller differences relative to the observations. A substantial reduction in MAD is observed along the Greenland, Barents Sea, and Svalbard regions. In contrast, ATLAS exhibits the largest differences to observations, with significant discrepancies persisting or even increasing along the ice edges in these areas.

https://doi.org/10.5194/egusphere-2026-6669
Preprint. Discussion started: 16 November 2026
© Author(s) 2026. CC BY 4.0 License.

The SIC increment maps show a general decrease in SIC across most ice-edge regions for all experiments (blue areas), with smaller regions of SIC increase (red). These increments primarily update the background along the ice edges, where high background MAD and significant model spread dominate. Through the covariance matrix, the assimilation of AMSR2 Tbs enables updates to other model variables, such as SIC. Consequently, SIC updates occur in regions where both the Tb (Fig. 9m-p) and SIC (Fig. 9l) background model ensembles exhibit significant spread, indicating high model uncertainty in both variables.

For ATLAS, positive SIC increments are observed near the MIZ in the Greenland, Barents Sea, and Svalbard regions (Fig. 9i), contrasting with the negative increments seen in other experiments. These positive increments result in higher MAD values in these areas, as noted earlier. The increments are driven by a significant underestimation of Tbs in the ATLAS background ensemble along the ice-edge regions (Fig. 9r), where the covariance matrix translates the Tb underestimation into positive SIC increments.

This background Tb underestimation in ATLAS near the MIZ is caused by the emissivity parameterization in the RTM, characterized by low or absent emissivity values in these regions. As described in Eq. 2, this substantially reduces the SIC-driven RTM Tb spread (Fig. 9n).

In contrast, for FIXED, DAL, and ML, the background overestimation of Tbs near the MIZ (Fig. 9q,s,t) arises from the generally higher sea-ice emissivity values used in these parameterizations compared to ATLAS for the same regions. In these cases, the SIC model ensemble (Fig. 9k) effectively drives the spread in RTM Tb simulations (Fig. 9m,o,p).

https://doi.org/10.5194/egusphere-2026-6669
Preprint. Discussion started: 16 November 2026
© Author(s) 2026. CC BY 4.0 License.

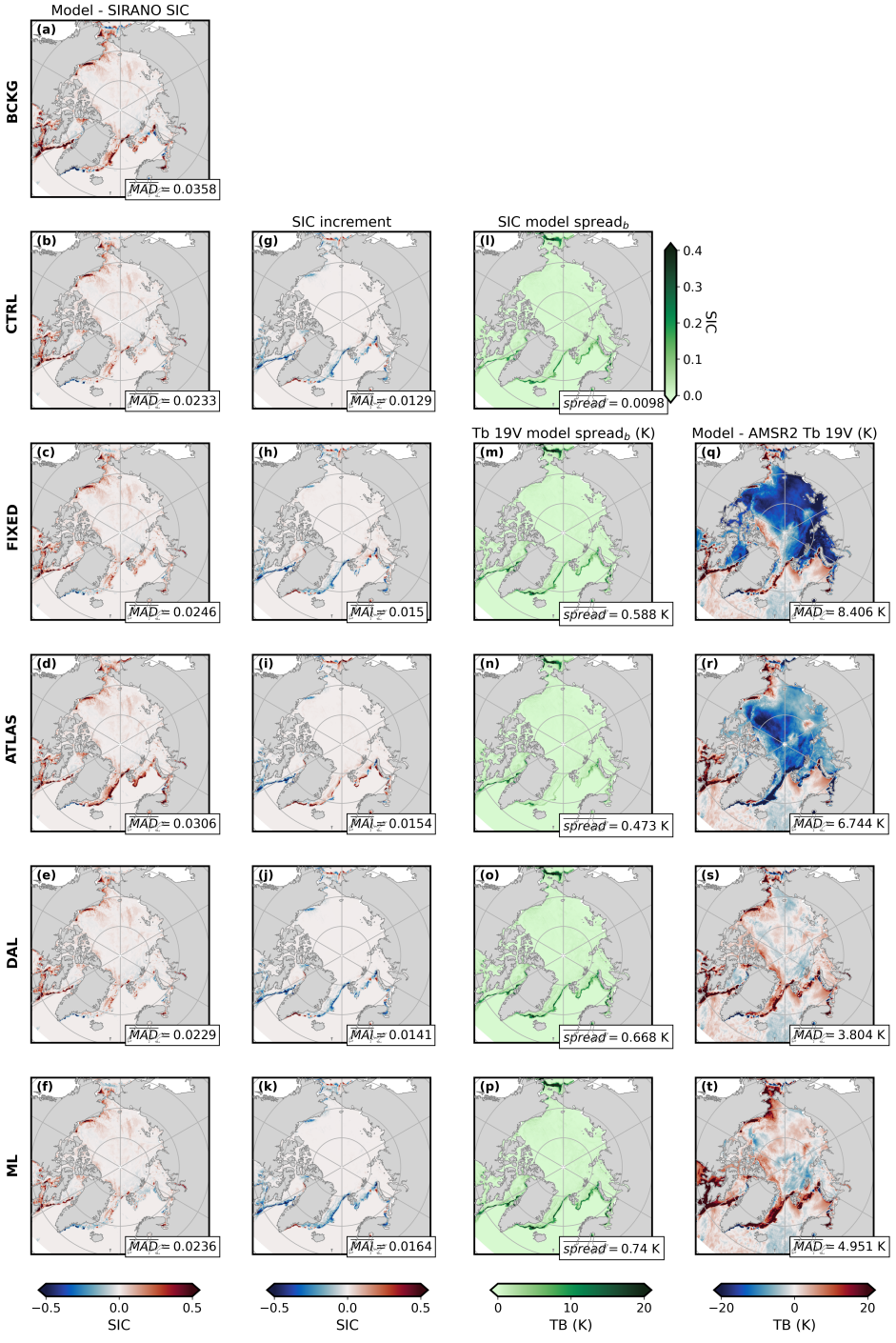


Figure 9. Maps of SIC model minus SIRANO SIC for the background (BCKG) model ensemble (a) and for the analysis ensembles (b–f); SIC increments (analysis minus background) (g–k); SIC background model spread (l); Tb 19V background model spread (m–p); and Tb 19V background difference to AMSR2 Tbs (q–t) for all experiments (CTRL, FIXED, ATLAS, DAL, ML). All fields correspond to data from 2024-01-15. Mean values of the difference to observations (mean absolute difference, MAD), SIC increment (mean absolute increment, MAI), and spread are provided in the top-right corner of each panel.

https://doi.org/10.5194/egusphere-2026-6669
Preprint. Discussion started: 16 November 2026
© Author(s) 2026. CC BY 4.0 License.

Figure 10 displays the spatial averages of various metrics computed within the numerical domain for each standalone analysis (represented by colored lines) over the six-month period. The metrics include: (i) the SIC MAD, which compares the
375 model analysis to the SIRANO SIC observations; (ii) the SIC absolute increment (analysis - background); (iii) DEnKF observation impact metrics; (iv) the SIT absolute increment. The total mean values of these metrics over the six-month period are summarized for each experiment in Tab. 3.

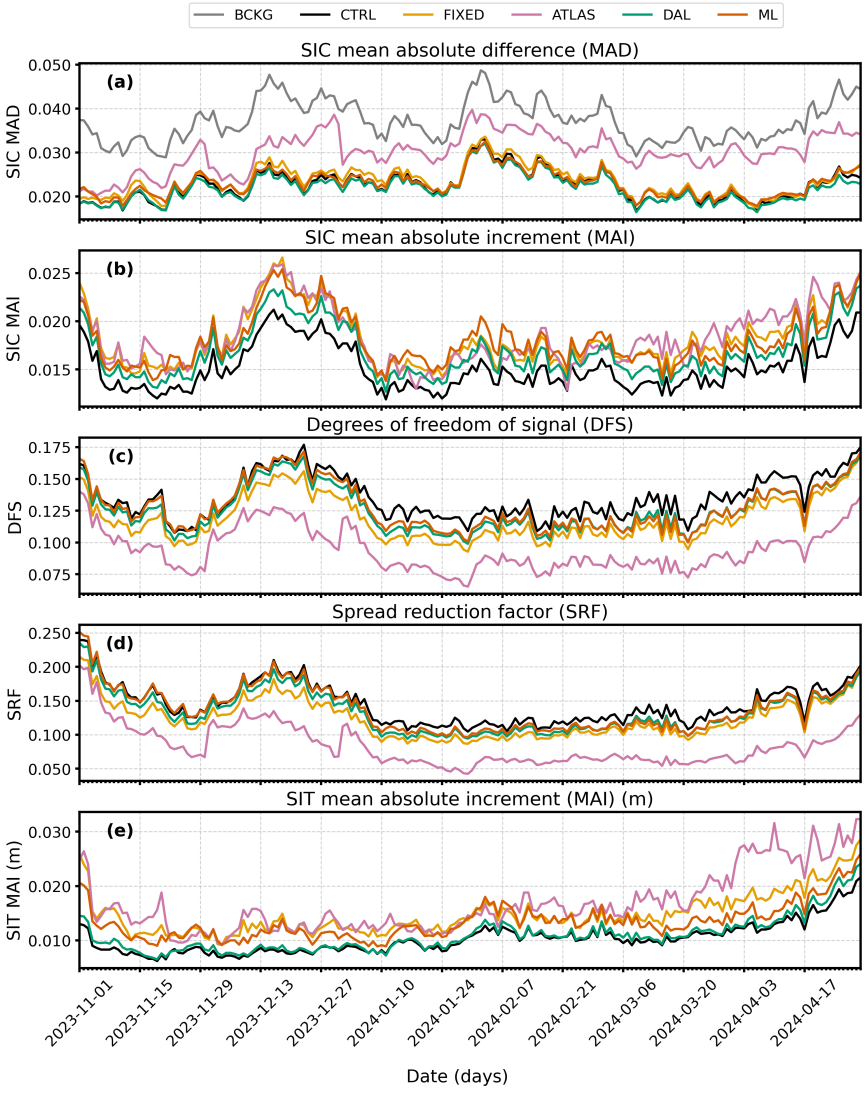


Figure 10. Spatial averages of the following metrics computed across all standalone analysis for all experiments over the six-month period from 1 November 2023 to 30 April 2024: (a) mean absolute difference (MAD) between the analysis and SIRANO SIC, (b) SIC mean absolute increment (MAI) with increment being the difference between analysis and background model ensemble data, (c) degrees of freedom of signal (DFS), (d) spread reduction factor (SRF), and (e) SIT mean absolute increment (MAI).

https://doi.org/10.5194/egusphere-2026-6669
Preprint. Discussion started: 16 November 2026
© Author(s) 2026. CC BY 4.0 License.

	BCKG	CTRL	FIXED	ATLAS	DAL	ML
SIC MAD	0.0371	0.0224	0.0235	0.0301	0.0219	0.0230
Reduction (%)	-	-39.62	-36.66	-18.87	-40.98	-38.01
SIC MAI	-	0.0151	0.0181	0.0184	0.0168	0.0180
DFS	-	0.1350	0.1187	0.0944	0.1258	0.1280
SRF	-	0.1447	0.1236	0.0837	0.1332	0.1380
SIT MAI (m)	-	0.0103	0.0147	0.0167	0.0109	0.0134

Table 3. Temporal averages of SIC metrics over a six-month period, including SIC mean absolute difference (MAD), percentage (%) reduction in MAD relative to the background, SIC mean absolute increment (MAI; analysis - background), degrees of freedom of signal (DFS), spatial reduction factor (SRF), and SIT mean absolute increment (MAI). For the background ensemble mean, only SIC MAD is presented, while all metrics are reported for the assimilation experiments: CTRL, FIXED, ATLAS, DAL, and ML.

The DEnKF analysis provides two key observation impact metrics: the degrees of freedom of signal (DFS) and the spread reduction factor (SRF). The DFS measures the effective number of independent pieces of information extracted from observations during the DA process. It quantifies the contribution of observations to updating the system state and is constrained by the smaller of two parameters: the number of assimilated observations or the number of ensemble members. Reducing the localization radius decreases the DFS, as it limits the number of observations contributing to the analysis. The SRF quantifies the reduction in ensemble spread (i.e., uncertainty) during the analysis step, reflecting the strength of the assimilation process. Increasing the observation error variance reduces the SRF. These metrics serve as internal diagnostics to evaluate the "health" of the assimilation system (Sakov et al., 2012). The DFS should typically remain below 1/3 to 1/2 of the ensemble size. A DFS that is too large may indicate rank deficiencies, suggesting that observations are over-constraining the system, reducing the assimilation sensitivity to observations. Similarly the SRF should remain below 1, as higher values may also indicate over-constraining effects. Different experiments yielding similar DFS and SRF metrics after analysis suggest that the observations are utilized in a comparable manner, highlighting their consistency and equivalence.

Figure 10 shows that all experiments reduce the SIC MAD across all analyses, with the largest reduction observed for DAL (-40.98%) and the smallest for ATLAS (-18.87%) averaged over all analyses. DAL achieves the strongest results, followed by CTRL, ML, and FIXED, while ATLAS provides the weakest performance. The CTRL experiment assimilates the SIRANO SIC observation itself, thus the MAD measures the "fit to observation", which provides a baseline for the strength of the DA update to the prior ensemble mean.

For SIC and SIT mean absolute increments (MAI), CTRL exhibits the lowest values throughout the entire period, followed by DAL. FIXED, ATLAS, and ML demonstrate similar SIC MAI values, although ATLAS shows significantly higher values from March onward, slightly increasing its overall temporal mean. While there are fluctuations in the MAI—such as periods where all experiments exhibit similar values (e.g., mid-January 2024) and periods of significant differences (e.g., mid-

https://doi.org/10.5194/egusphere-2026-6669
Preprint. Discussion started: 16 November 2026
© Author(s) 2026. CC BY 4.0 License.

December 2023)—the resulting MAD after analysis behaves quite consistently across experiments, with ATLAS consistently underperforming.

As previously discussed, the majority of SIC updates occur near the ice edge, where ensemble spread is substantial. Although ATLAS background Tbs exhibit larger errors in these regions compared to other RTM configurations, the Tb ensemble spread in much of the ice edge remains weak. This results in inaccurate but small Tb updates. In these areas, erroneous Tb increments lead to positive SIC increments where negative increments are required, ultimately increasing the overall MAD.

This can be attributed to the fact that the RTM, particularly when using suboptimal emissivity parameterizations, introduces additional mismatches in the background relative to the observations. As a result, the innovation (observation minus background) becomes larger, leading to greater analysis increments. However, these larger increments do not necessarily result in a closer fit to the SIRANO SIC in the analysis, as evidenced by the MAD values.

Figure A4 shows SIT increment fields for each experiment on 2024-01-15. The FIXED experiment exhibits significant positive SIT increments in regions closer to the ice pack, while ATLAS again shows positive increments near the Greenland and Barents Sea, where other experiments display negative increments. CTRL, DAL, and ML present similar spatial patterns of SIT increments, with ML showing larger negative increments along the Greenland and Barents Sea regions.

A strong overall correlation was observed between DFS, SRF, and SIC increments across all experiments. This is expected, as these metrics reflect the impact of observations in the analysis and are inherently linked to SIC increments. Among all experiments, CTRL consistently exhibited the highest values for these metrics throughout the six-month period. While DAL and ML showed similar DFS values to CTRL during November and December, all experiments consistently reported lower DFS and SRF values than CTRL, with ATLAS displaying the lowest values.

The reduced DFS and SRF values in the experiments (compared to CTRL) can be attributed to the use of the RTM in relating the observed Tbs to SIC, the variable being updated. This process reduces the observation-state correlation, thereby diminishing the impact of observations through the Kalman gain. However, DAL and ML, with their improved emissivity parameterizations, achieve observation impacts closer to those of CTRL. In contrast, ATLAS reports significantly lower values for these metrics, which can be explained by the reduced spread of RTM Tbs in certain regions, leading to a decreased influence of observations.

Since the DAL parameterization incorporates information from AMSR2 Tbs over the seven days preceding the analysis (including the analysis date; see details in Subsect. 4.2), tests were conducted to evaluate the temporal dependence of this parameterization. Specifically, the coefficients and DAL fields used in the sea-ice emissivity computation were varied by utilizing data from one day, seven days, and 28 days prior to the analysis. Over the six-month period, the results showed a reduction in the background error of 41.09% for data from one day prior, 41.03% for seven days prior, and 41.83% for 28 days prior. These results demonstrate minimal variation in the reduction percentages across the tested time frames.

This consistency can be attributed to the relatively stable nature of MYI and FYI areas during the single winter season studied. Consequently, using DAL information derived from AMSR2 data that is up to one month old is a valid approach for computing sea-ice emissivity.

https://doi.org/10.5194/egusphere-2026-6669
Preprint. Discussion started: 16 November 2026
© Author(s) 2026. CC BY 4.0 License.

6.3 Regional evaluation of the analysis

We compute the MAD values between the model analysis and SIRANO SIC for all experiments across different regions: the total area (All), MYI, FYI, and MIZ. The temporal averages over the six-month period are shown in Tab. 4.

For the total area, all experiments reduce the background MAD, with DAL achieving the lowest value, followed closely by CTRL. While the other experiments show slightly higher MAD values, they still reduce the background MAD by approximately 40%, except for ATLAS, which exhibits the weakest performance with a reduction of only $\sim 19\%$.

	All	% Red.	MYI	% Red.	FYI	% Red.	MIZ	% Red.
BCKG	0.0371	-	0.0174	-	0.0569	-	0.3150	-
CTRL	0.0224	39.62	0.0143	17.82	0.0329	42.16	0.1850	41.27
FIXED	0.0235	36.55	0.0170	2.30	0.0359	36.88	0.1773	43.73
ATLAS	0.0301	18.86	0.0170	2.30	0.0462	18.81	0.2705	14.13
DAL	0.0219	41.00	0.0151	13.22	0.0326	42.69	0.1737	44.85
ML	0.0230	38.00	0.0174	0.00	0.0347	39.01	0.1725	45.25

Table 4. Mean temporal values of SIC mean absolute difference (MAD) compared to the SIRANO SIC product over a six-month period, including percentage (%) MAD reduction relative to the background (BCKG) for each region: total area (All), multi-year ice (MYI), first-year ice (FYI), and marginal ice zone (MIZ). The BCKG row provides the reference MAD values, while percentage reductions are presented for the assimilation experiments: CTRL, FIXED, ATLAS, DAL, and ML.

In the MYI region, the updates are notably weaker due to the low model spread in this area. Among the experiments, CTRL achieves the strongest performance, reducing the background MAD by 17.82%, followed by DAL with a 13.22% reduction. The other parameterizations, however, show MAD values that are significantly closer to the background.

In the FYI region, DAL and CTRL perform similarly, achieving a substantial reduction of approximately 42% in the background MAD. ML and FIXED follow closely, with reductions that are 3–5% weaker. ATLAS, on the other hand, exhibits a noticeably higher MAD compared to the other experiments, though it still outperforms the background.

In the MIZ, where the largest background errors are observed, ML achieves the lowest MAD, closely followed by DAL and FIXED, all of which outperform CTRL. In this region, all experiments reduce the background MAD by approximately 41-45%, except for ATLAS, which achieves a much weaker reduction of only $\sim 14\%$. Notably, the Tb-assimilation experiments (excluding ATLAS) provide additional reductions of approximately 0.010 compared to CTRL, with ML standing out by delivering a 4% stronger reduction.

We further evaluate the SIC analysis from the offline DA experiments by comparing it against the Bremen ASI SIC product (see Tab.5). The Bremen ASI product is also derived from AMSR2 Tb observations but utilizes a different frequency channel (89 GHz) and a distinct algorithm. Consequently, the resulting SIC product exhibits some differences compared to SIRANO.

https://doi.org/10.5194/egusphere-2026-6669
Preprint. Discussion started: 16 November 2026
© Author(s) 2026. CC BY 4.0 License.

Since CTRL assimilates SIRANO SIC, comparing its analysis to the assimilated observations (SIRANO) provides an inherently favorable comparison, making it less objective than comparisons to other SIC products such as Bremen.

	All	% Red.	MYI	% Red.	FYI	% Red.	MIZ	% Red.
BCKG	0.0411	-	0.0184	-	0.0651	-	0.3561	-
CTRL	0.0308	25.06	0.0174	5.43	0.0505	22.43	0.2596	27.08
FIXED	0.0298	27.49	0.0201	-9.24	0.0481	26.11	0.2392	32.81
ATLAS	0.0337	18.01	0.0166	9.78	0.0531	18.42	0.3302	7.27
DAL	0.0295	28.24	0.0180	2.17	0.0493	24.26	0.2311	35.08
ML	0.0308	25.06	0.0208	-13.04	0.0518	20.43	0.2266	36.37

Table 5. Mean temporal values of SIC mean absolute difference (MAD) compared to the Bremen ASI SIC product over a six-month period, including percentage (%) MAD reduction relative to the background (BCKG) for each region: total area (All), multi-year ice (MYI), first-year ice (FYI), and marginal ice zone (MIZ). The BCKG row provides the reference MAD values, while percentage reductions are presented for the assimilation experiments: CTRL, FIXED, ATLAS, DAL, and ML.

Due to differences between the SIC products, the background MAD over the six-month period is 0.0411 when compared to Bremen ASI, which is 11% higher than the 0.0371 MAD observed when compared to SIRANO. These discrepancies are most pronounced in sea-ice areas near the MIZ (see Fig. A1c). In these regions, the Bremen product generally overestimates SIC compared to SIRANO. Conversely, at the MIZ boundary, SIRANO typically reports higher SIC values than Bremen.

When compared to the Bremen ASI product, the overall MAD reductions relative to background are weaker than those observed against SIRANO, but the analysis results remain consistent.

Across the entire region, all experiments reduce the background MAD, with most achieving reductions of 25–28%, except for ATLAS, which achieves only 18%. DAL achieves the largest MAD reduction across the region. In MYI areas, where updates are minimal, the background MAD reduction is limited. In FYI areas, FIXED and DAL show the smallest differences after analysis.

In the MIZ, which sees the strongest updates, all experiments (except ATLAS) achieve reductions above 27% relative to the background MAD. Tb-assimilation consistently results in a closer fit to observations than CTRL, particularly in the MIZ, with a 5–9% MAD reduction. ML shows the strongest performance in this region.

Compared to the previous analysis against SIRANO, DAL now shows more than a 3% reduction in MAD across the entire region (compared to $\sim 1.5\%$ against SIRANO), while ML achieves a 9% reduction in the MIZ (up from 4% in the SIRANO comparison).

https://doi.org/10.5194/egusphere-2026-6669
Preprint. Discussion started: 16 November 2026
© Author(s) 2026. CC BY 4.0 License.

7 Discussion and conclusions

The direct assimilation of AMSR2 Tbs in the Arctic is evaluated using offline analyses to update TOPAZ5 ensemble SIC and SIT fields. Model Tbs are generated with a forward RTM and updated via DEnKF analysis. Among tested parameterizations, the DAL emissivity parameterization yields the smallest difference between RTM and AMSR2 Tbs. Assimilating AMSR2 Tbs with DAL outperforms SIRANO SIC assimilation, achieving lower differences to SIRANO SIC, supported by comparisons with Bremen ASI SIC. In the MIZ, Tb-assimilation (except ATLAS) consistently outperforms SIC-assimilation, reducing mean absolute difference (MAD) values by 2–9% relative to both SIC products.

In the RTM evaluation, we test four sea-ice emissivity parameterizations: FIXED, ATLAS, DAL, and ML. The DAL parameterization produces RTM Tbs with the smallest differences compared to AMSR2 Tbs and provides good differentiation between MYI and FYI areas. While ML shows larger differences from observations than DAL, it effectively represents the spatial variability of Tbs. Both DAL and ML exhibit a mix of over- and underestimation, with a tendency to overestimate near the ice edge. The FIXED parameterization, using constant sea-ice emissivity, overlooks ice-type variability, leading to overestimation over MYI and underestimation over FYI. ATLAS, derived from monthly climatology, captures some spatial variability, with lower emissivity values in MYI regions and higher values in FYI areas. However, overly low emissivity values in MYI regions lead to significant underestimation of RTM ATLAS Tbs. Additionally, the Atlas climatology assigns low or null emissivity near ice edges, causing further underestimation, especially during winter when sea-ice extent is largest. This makes ATLAS the weakest parameterization in the MIZ, while FIXED performs comparably to DAL and ML in this region. Strong performance in the MIZ is particularly important for assimilation studies, as model background errors and spread are typically concentrated in this area.

Across 182 standalone analyses, DAL achieves the largest SIC MAD reduction (41%) relative to the background difference compared to SIRANO, even when relying on outdated AMSR2 Tb data for effective emissivity computation. Other experiments perform slightly worse (<40%), with ATLAS showing the weakest reduction (<19%). In MYI regions, CTRL (SIC-assimilation) produces the most significant SIC updates, followed by DAL, although updates remain minimal due to the low model spread. High spread for SIC and Tb is primarily observed in FYI areas, particularly in the MIZ, where most updates occur. In the MIZ, all Tb-assimilation experiments (except ATLAS) outperform SIC-assimilation, with ML delivering the strongest performance, closely followed by DAL. These findings are consistent with comparisons to other SIC products, such as Bremen ASI, underscoring the advantages of assimilating raw satellite Tb over SIC.

The RTM Tbs derived from TOPAZ5 SIC data exhibit a similar spread pattern to the TOPAZ5 SIC ensemble, reflecting regions of high and low spread due to the strong linear relationship between Tbs and SIC in the RTM. In contrast, the RTM ATLAS ensemble shows low Tb spread in the Greenland and Barents Seas, driven by low emissivity values and data scarcity. This leads to consistently underestimated ATLAS Tbs across all members in these regions, resulting in large positive SIC increments in the DEnKF analysis where negative increments are expected.

https://doi.org/10.5194/egusphere-2026-6669
Preprint. Discussion started: 16 November 2026
© Author(s) 2026. CC BY 4.0 License.

In the DAL experiment, SIT increments are slightly higher than in CTRL but remain focused near the MIZ. In contrast, other Tb-assimilation experiments show significant increments in small areas within the ice pack, highlighting the potential of Tb assimilation to deliver stronger updates to sea-ice type and thickness values.

Assimilating Tbs incurs a slightly higher computational cost compared to SIC assimilation, primarily due to the larger number of observations (four Tb channels) and, to a lesser extent, the use of the RTM to simulate model Tbs. However, the DEnKF algorithm computes observation priors (Tbs) in parallel, resulting in only a minor increase in wall-clock time. Additionally, the assimilation algorithm is not sensitive to the number of observations, making the direct assimilation of Tbs feasible for operational use.

This study focuses on the winter period, as summer poses challenges such as lower SIC and melt ponds. Positive results with RTM have been observed in summer, with DAL outperforming FIXED (results not shown). Preliminary summer findings suggest that Tb-assimilation with DAL reduces overfitting to biased SIC caused by atmospheric noise, improving ice edge and overall ice condition representation compared to SIC-assimilation.

To perform summer assimilation with the ML parameterization, the data-driven algorithm would need to be trained on summer data. However, predictions may be less accurate due to the reduced correlation between surface emissivities and sea ice type in the presence of melt ponds. In this study, the algorithm is trained on data from only two winters. Broader applicability would require training over a longer period (e.g., 10 winters) to enhance prediction accuracy and expand spatial coverage of the predicted sea-ice emissivities.

The AMSR2 data can be assimilated asynchronously by assimilating the passes instead of the spatial means (Durán Moro et al., 2024); tests were successfully performed but due to limit storage capacity in this study we focus on the assimilation of daily means of AMSR2 Tb and SIC.

While this analysis is conducted in the Arctic, the methodology could also be applied to the Southern Ocean (SO). Characterized by FYI, a broader MIZ, and significant seasonal variability, assimilation in the SO could focus on winter, when sea ice is more stable. The primary challenge lies in capturing rapid MIZ changes driven by interactions with open water and atmospheric variability. However, the simpler RTM Tb simulations under predominantly FYI conditions make the SO less complex compared to the Arctic. For DAL, new coefficients would need to be computed using data specific to the SO. Since no equivalent climatology exists in this region, ATLAS cannot be applied. FIXED parameterization could be explored by reviewing the literature and identifying FYI emissivity values specific to the SO. ML parameterization, however, would require training the algorithm with regional data using a different model, as TOPAZ5 is designed for the Arctic.

Future work will focus on updating sea-ice type information in model variables such as sea-ice age and thickness using data-driven techniques. The RTM will be examined with perturbations in atmospheric fields to deviate from the linear relationship between Tb and SIC. Additionally, the RTM used in this study is a simplified version, and further development is planned to enable the assimilation of Tbs onto other ocean variables, such as sea-surface temperature and salinity.

This study's investigation of directly assimilating AMSR2 Tbs to improve model sea-ice fields represents an important first step in preparing for the upcoming Copernicus Imaging Microwave Radiometer (CIMR) mission. It also highlights a promising path toward coupled assimilation in integrated atmosphere-ice-ocean models.

https://doi.org/10.5194/egusphere-2026-6669
Preprint. Discussion started: 16 November 2026
© Author(s) 2026. CC BY 4.0 License.

Code and data availability. The source code for the EnKF-C v.2.9.9 is obtained from https://github.com/sakov/EnKF-C.git, commit *7eea4d8* as of Jul 8, 2021. SIRANO and model data from CTRL, FIXED, ATLAS, DAL and ML experiments will be made available in the public server host by the Norwegian Meteorological Institute. Specific EnKF-C parameters files used for these experiments will be archived at Zenodo. Radiative transfer model code is openly available through GitHub (https://github.com/marinadmo/rtm_da).

Appendix A

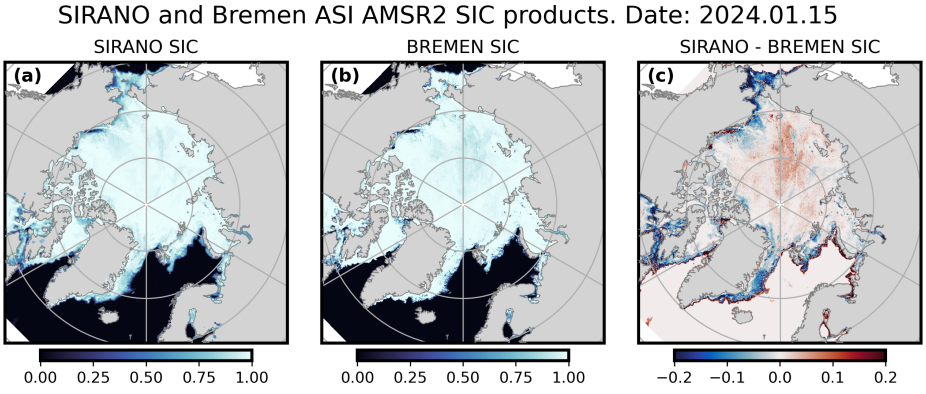


Figure A1. SIRANO and Bremen ASI SIC products on 15 January 2024 and their difference.

https://doi.org/10.5194/egusphere-2026-6669
Preprint. Discussion started: 16 November 2026
© Author(s) 2026. CC BY 4.0 License.

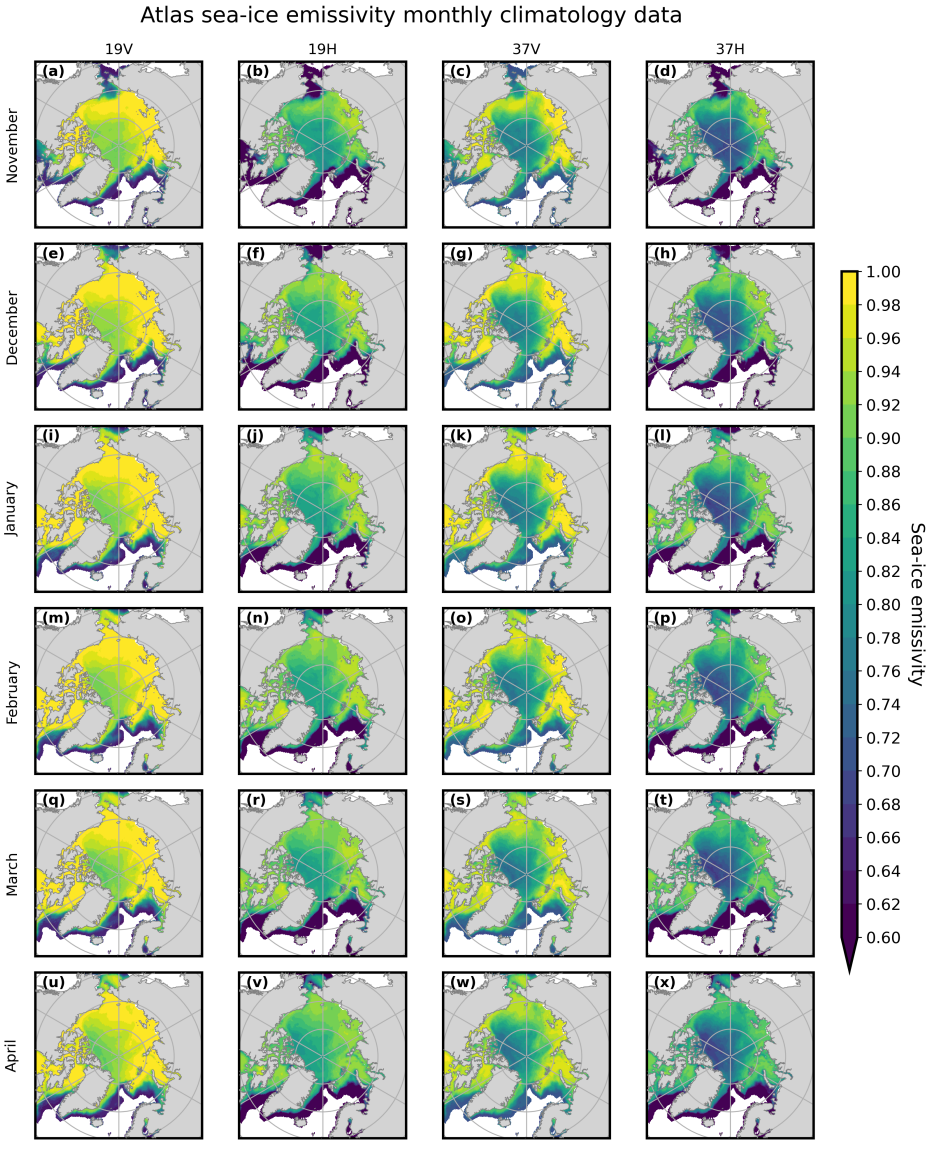


Figure A2. Atlas sea-ice emissivity monthly climatology fields from November (a-d), December (e-h), January (i-l), February (m-p), March (g-t), and April (u-x) for each channel (19V, 19H, 37V, 37H). Areas where Atlas emissivities are zero are masked out.

https://doi.org/10.5194/egusphere-2026-6669
Preprint. Discussion started: 16 November 2026
© Author(s) 2026. CC BY 4.0 License.

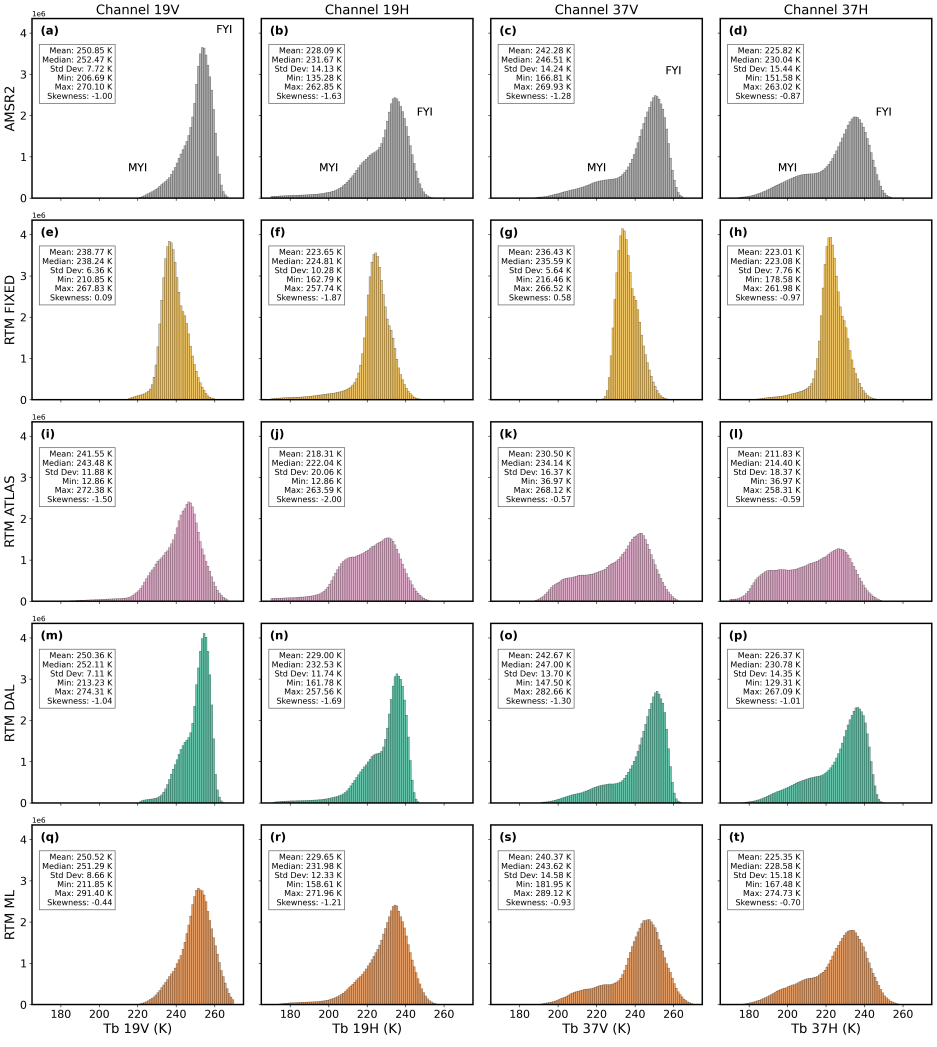


Figure A3. Histograms of AMSR2 (a-d) and RTM Tbs for FIXED (e-h), ATLAS (i-l), DAL (m-p), and ML (g-t) parameterizations for each channel (19V, 19H, 37V, 37H) over areas with SIC $> 50\%$. Left top box indicates statistics on each Tb dataset.

https://doi.org/10.5194/egusphere-2026-6669
Preprint. Discussion started: 16 November 2026
© Author(s) 2026. CC BY 4.0 License.

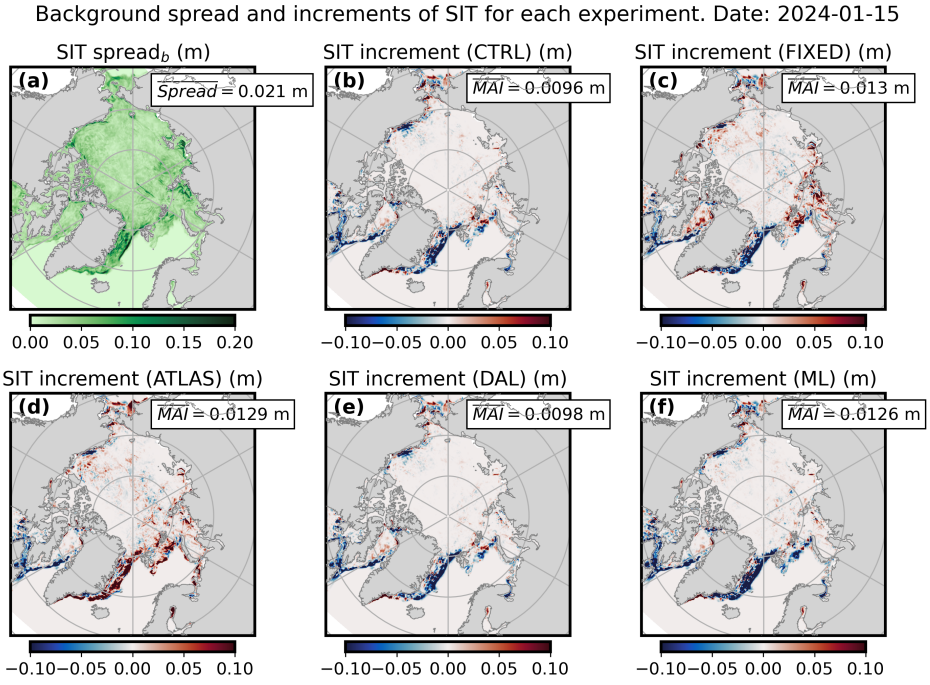


Figure A4. Maps of background ensemble spread of SIT (a) and increments of SIT for CTRL (b), FIXED (c), ATLAS (d), DAL (e) and ML (f) experiments on 2024-01-15.

Author contributions. MDM: conceptualization, methodology, investigation and software (experiments setup and implementation), formal data analysis and visualization, writing – original draft preparation and writing - review & editing. TL: conceptualization, methodology, formal data analysis, supervision (Work Package leader), software (SIRANO observations), writing - review & editing. LB: conceptualization, methodology, funding acquisition, project administration (project manager), supervision, writing - review & editing. CP: software (machine learning), writing - review & editing. YY: formal data analysis, writing - review & editing. JX: writing - review & editing. AMS: software (SIRANO observations), data preparation.

Competing interests. There are no competing interests associated with this work.

Acknowledgements. We acknowledge funding by the Horizon EU, grant No. 101081568 (ACCIBERG). This study has been conducted using E.U. Copernicus Marine Service Information: TOPAZ5 10-days forecast (https://doi.org/10.48670/moi-00001). We acknowledge the R&D contribution of ESA CCI Sea Ice and EUMETSAT OSI SAF projects to the preparation of the regional SIC product. We are particularly grateful to Pavel Sakov for the technical support and help with the use of the EnKF-C software.

https://doi.org/10.5194/egusphere-2026-6669
Preprint. Discussion started: 16 November 2026
© Author(s) 2026. CC BY 4.0 License.

References

Aaboe, S., Down, E., Sørensen, A., Lavergne, T., and Eastwood, S.: Sea-ice type climate data record 1978-present, v4.0, https://doi.org/10.24381/cds.29c46d83, accessed on 01-06-2026, 2026.

Aires, F., Prigent, C., Bernardo, F., Jiménez, C., Saunders, R., and Brunel, P.: A Tool to Estimate Land-Surface Emissivities at Microwave frequencies (TELSEM) for use in numerical weather prediction, Quarterly Journal of the Royal Meteorological Society, 137, 690–699, https://doi.org/https://doi.org/10.1002/qj.803, 2011.

Ali, A., Burud, A., Melsom, A., Bertino, L., Xie, J., and Sumata, H.: Product user manual for Arctic ocean physical analysis and forecasting product, https://doi.org/10.48670/moi-00001, 2025.

Bertino, L., Ali, A., Carrasco, A., Lien, V., and Melsom, A.: THE ARCTIC MARINE FORECASTING CENTER IN THE FIRST COPERNICUS PERIOD, in: 9th EuroGOOS International Conference, Shom; Ifremer; EuroGOOS AISBL, pp. 256–263, Brest, France, https://hal.archives-ouvertes.fr/hal-03334274v2/document, hal-03334274v2, 2021.

Bertino, L., Heimbach, P., Blockley, E., and Ólason, E.: Numerical models for monitoring and forecasting sea ice: a short description of present status, State of the Planet, 5-opsr, 14, https://doi.org/10.5194/sp-5-opsr-14-2025, 2025.

Bleck, R.: An oceanic general circulation model in pressure coordinates, Ocean Model., 37, 55–88, https://doi.org/10.1016/S1463-5003(01)00012-9, 2002.

Cheng, S., Chen, Y., Aydoğdu, A., Bertino, L., Carrassi, A., Rampal, P., and Jones, C. K. R. T.: Arctic sea ice data assimilation combining an ensemble Kalman filter with a novel Lagrangian sea ice model for the winter 2019–2020, The Cryosphere, 17, 1735–1754, https://doi.org/10.5194/tc-17-1735-2023, 2023.

Comiso, J. C.: Large Decadal Decline of the Arctic Multiyear Ice Cover, Journal of Climate, 25, 1176 – 1193, https://doi.org/10.1175/JCLI-D-11-00113.1, 2012.

Durán Moro, M., Sperrevik, A. K., Lavergne, T., Bertino, L., Gusdal, Y., Iversen, S. C., and Rusin, J.: Assimilation of satellite swaths versus daily means of sea ice concentration in a regional coupled ocean–sea ice model, The Cryosphere, 18, 1597–1619, https://doi.org/10.5194/tc-18-1597-2024, 2024.

Eppler, D. T., Farmer, L. D., Lohanick, A. W., Anderson, M. R., Cavalieri, D. J., Comiso, J., Gloersen, P., Garrity, C., Grenfell, T. C., Hallikainen, M., Maslanik, J. A., MäTzler, C., Melloh, R. A., Rubinstein, I., and Swift, C. T.: Passive Microwave Signatures of Sea Ice, chap. 4, pp. 47–71, American Geophysical Union (AGU), ISBN 9781118663950, https://doi.org/https://doi.org/10.1029/GM068p0047, 1992.

Evensen, G.: Inverse methods and data assimilation in nonlinear ocean models, Physica D: Nonlinear Phenomena, 77, 108–129, https://doi.org/10.1016/0167-2789(94)90130-9, 1994.

Evensen, G.: The Ensemble Kalman Filter: theoretical formulation and practical implementation, Ocean Dynamics, 53, 343–367, https://doi.org/10.1007/s10236-003-0036-9, 2003.

Geer, A. J.: Simultaneous Inference of Sea Ice State and Surface Emissivity Model Using Machine Learning and Data Assimilation, Journal of Advances in Modeling Earth Systems, 16, e2023MS004 080, https://doi.org/https://doi.org/10.1029/2023MS004080, e2023MS004080 2023MS004080, 2024.

Gunnarsson, B.: Recent ship traffic and developing shipping trends on the Northern Sea Route – Policy implications for future arctic shipping, Marine Policy, 124, 104 369, https://doi.org/10.1016/j.marpol.2020.104369, 2021.

https://doi.org/10.5194/egusphere-2026-6669
Preprint. Discussion started: 16 November 2026
© Author(s) 2026. CC BY 4.0 License.

Hersbach, H., Bell, B., Berrisford, P., Biavati, G., Horányi, A., Muñoz Sabater, J., Nicolas, J., Peubey, C., Radu, R., Rozum, I., Schepers, D., Simmons, A., Soci, C., Dee, D., and Thépaut, J.-N.: ERA5 hourly data on single levels from 1940 to present, https://doi.org/10.24381/cds.adbb2d47, accessed on 01-01-2024, 2023.

Hunke, E. C., Lipscomb, W. H., Turner, A. K., Jeffery, N., and Elliott, S.: CICE: The Los Alamos sea ice model documentation and software user's manual, Version 5, https://www.cesm.ucar.edu/models/cesm2/sea-ice, 2015.

Ivanova, N., Pedersen, L. T., Tonboe, R. T., Kern, S., Heygster, G., Lavergne, T., Sørensen, A., Saldo, R., Dybkjær, G., Brucker, L., and Shokr, M.: Inter-comparison and evaluation of sea ice algorithms: towards further identification of challenges and optimal approach using passive microwave observations, The Cryosphere, 9, 1797–1817, https://doi.org/10.5194/tc-9-1797-2015, 2015.

Kern, S., Lavergne, T., Notz, D., Pedersen, L. T., Tonboe, R. T., Saldo, R., and Sørensen, A. M.: Satellite passive microwave sea-ice concentration data set intercomparison: closed ice and ship-based observations, The Cryosphere, 13, 3261–3307, https://doi.org/10.5194/tc-13-3261-2019, 2019.

Kilic, L., Jimenez, C., Prigent, C., Korosov, A., Rampal, P., de Gelis, I., and Garric, G.: Parameterization of the Winter Arctic Sea Ice Microwave Emissivity Between 1.4 and 36 GHz, for Large Scale Applications, Earth and Space Science, 12, e2025EA004 259, https://doi.org/https://doi.org/10.1029/2025EA004259, e2025EA004259 2025EA004259, 2025.

Lavergne, T., Sørensen, A. M., Kern, S., Tonboe, R., Notz, D., Aaboe, S., Bell, L., Dybkjær, G., Eastwood, S., Gabarro, C., Heygster, G., Killie, M. A., Brandt Kreiner, M., Lavelle, J., Saldo, R., Sandven, S., and Pedersen, L. T.: Version 2 of the EUMETSAT OSI SAF and ESA CCI sea-ice concentration climate data records, The Cryosphere, 13, 49–78, https://doi.org/10.5194/tc-13-49-2019, 2019.

Mathew, N., Heygster, G., and Melsheimer, C.: Surface Emissivity of the Arctic Sea Ice at AMSR-E Frequencies, IEEE Transactions on Geoscience and Remote Sensing, 47, 4115–4124, https://doi.org/10.1109/TGRS.2009.2023667, 2009.

Meissner, T. and Wentz, F.: An updated analysis of the ocean surface wind direction signal in passive microwave brightness temperatures, IEEE Transactions on Geoscience and Remote Sensing, 40, 1230–1240, https://doi.org/10.1109/TGRS.2002.800231, 2002.

Meissner, T. and Wentz, F.: The complex dielectric constant of pure and sea water from microwave satellite observations, IEEE Transactions on Geoscience and Remote Sensing, 42, 1836–1849, https://doi.org/10.1109/TGRS.2004.831888, 2004.

Meissner, T. and Wentz, F.: Ocean Retrievals for WindSat, in: 2006 IEEE MicroRad, pp. 119–124, https://doi.org/10.1109/MICRAD.2006.1677074, 2006.

Meissner, T. and Wentz, F.: The emissivity of the ocean surface between 6 and 90 GHz over a large range of wind speeds and Earth incidence angles, IEEE Transactions on Geoscience and Remote Sensing, 50, 3004–3026, https://doi.org/10.1109/tgrs.2011.2179662, 2012.

Melsheimer, C.: ASI Version 5 Sea Ice Concentration User Guide, Institute of Environmental Physics, University of Bremen, https://data.seaice.uni-bremen.de/amsr2/ASIuserguide.pdf, 2024.

Müller, M., Knol-Kauffman, M., Jeuring, J., and Palerme, C.: Arctic shipping trends during hazardous weather and sea-ice conditions and the Polar Code's effectiveness, npj Ocean Sustainability, 2, https://doi.org/10.1038/s44183-023-00021-x, 2023.

Othmani, A., Samuelsen, A., Xie, J., Bertino, L., Mangini, F., and Raj, R. P.: TOPAZ5: A high-resolution ocean and sea-ice model for the Arctic and North Atlantic, EGUsphere [preprint], https://doi.org/10.5194/egusphere-2026-1520, 2026.

Prigent, C., Rossow, W. B., and Matthews, E.: Microwave land surface emissivities estimated from SSM/I observations, Journal of Geophysical Research: Atmospheres, 102, 21 867–21 890, https://doi.org/https://doi.org/10.1029/97JD01360, 1997.

Rusin, J., Lavergne, T., Doulgeries, A. P., and Scott, K. A.: Resolution enhanced sea ice concentration: a new algorithm applied to AMSR2 microwave radiometry data, Annals of Glaciology, p. 1–37, https://doi.org/10.1017/aog.2024.6, 2024.

Sakov, P.: EnKF-C user guide, https://doi.org/10.48550/ARXIV.1410.1233, 2014.

https://doi.org/10.5194/egusphere-2026-6669
Preprint. Discussion started: 16 November 2026
© Author(s) 2026. CC BY 4.0 License.



Sakov, P. and Oke, P. R.: A deterministic formulation of the ensemble Kalman filter: an alternative to ensemble square root filters, Tellus A, 60, 361–371, https://doi.org/10.1111/j.1600-0870.2007.00299.x, 2008.

Sakov, P., Counillon, F., Bertino, L., Lisæter, K. A., Oke, P. R., and Korablev, A.: TOPAZ4: An ocean–sea ice data assimilation system for the North Atlantic and Arctic, Ocean Sci., 8, 633–656, https://doi.org/10.5194/os-8-633-2012, 2012.

Scarlat, R. C., Heygster, G., and Pedersen, L. T.: Experiences With an Optimal Estimation Algorithm for Surface and Atmospheric Parameter Retrieval From Passive Microwave Data in the Arctic, IEEE Journal of Selected Topics in Applied Earth Observations and Remote Sensing, 10, 3934–3947, https://doi.org/10.1109/JSTARS.2017.2739858, 2017.

Scarlat, R. C., Spreen, G., Heygster, G., Huntemann, M., Paţilea, C., Pedersen, L. T., and Saldo, R.: Sea Ice and Atmospheric Parameter Retrieval From Satellite Microwave Radiometers: Synergy of AMSR2 and SMOS Compared With the CIMR Candidate Mission, Journal of Geophysical Research: Oceans, 125, e2019JC015 749, https://doi.org/https://doi.org/10.1029/2019JC015749, e2019JC015749 10.1029/2019JC015749, 2020.

Scott, K. A., Buehner, M., Caya, A., and Carrieres, T.: Direct Assimilation of AMSR-E Brightness Temperatures for Estimating Sea Ice Concentration, Monthly Weather Review, 140, 997 – 1013, https://doi.org/10.1175/MWR-D-11-00014.1, 2012.

Spreen, G., Kaleschke, L., and Heygster, G.: Sea ice remote sensing using AMSR-E 89-GHz channels, Journal of Geophysical Research: Oceans, 113, C02S03, https://doi.org/10.1029/2005JC003384, 2008.

Stocker, A. N., Renner, A. H., and Knol-Kauffman, M.: Sea ice variability and maritime activity around Svalbard in the period 2012–2019, Scientific Reports, 10, 17 043, https://doi.org/10.1038/s41598-020-74064-2, 2020.

Tonboe, R. T., Eastwood, S., Lavergne, T., Sørensen, A. M., Rathmann, N., Dybkjær, G., Pedersen, L. T., Høyer, J. L., and Kern, S.: The EUMETSAT sea ice concentration climate data record, The Cryosphere, 10, 2275–2290, https://doi.org/10.5194/tc-10-2275-2016, 2016.

Wang, D., Prigent, C., Kilic, L., Fox, S., Harlow, C., Jimenez, C., Aires, F., Grassotti, C., and Karbou, F.: Surface Emissivity at Microwaves to Millimeter Waves over Polar Regions: Parameterization and Evaluation with Aircraft Experiments, Journal of Atmospheric and Oceanic Technology, 34, 1039 – 1059, https://doi.org/10.1175/JTECH-D-16-0188.1, 2017.

Wentz, F. and Meissner, T.: Algorithm theoretical basis document: AMSR ocean algorithm, version 2, Technical Report 121599A-1, Remote Sensing Systems, Santa Rosa, CA, https://images.remss.com/papers/rsstech/2000_121599A-1_Wentz_AMSR_Ocean_ATBD_V2.pdf, accessed: 2025-06-25, 2000.

Xie, J., Bertino, L., Counillon, F., Lisæter, K. A., and Sakov, P.: Quality assessment of the TOPAZ4 reanalysis in the Arctic over the period 1991–2013, Ocean Science, 13, 123–144, https://doi.org/10.5194/os-13-123-2017, 2017.

Yan, Z., Ye, Y., Heygster, G., Chen, Z., Yu, Z., Han, Y., and Cheng, X.: Integrated Retrieval of Ice, Ocean, and Atmospheric Variables With an Emissivity Corrected Optimal Estimation Method in the Arctic, IEEE Transactions on Geoscience and Remote Sensing, 64, 4301 415–4301 415, https://doi.org/10.1109/TGRS.2026.3696269, 2026.